

REPORT DOCUMENTATION PAGE				Form Approved OMB No. 0704-0188	
Public reporting burden for this collection of information is estimated to average 1 hour per response, including the time for reviewing instructions, searching existing data sources, gathering and maintaining the data needed, and completing and reviewing this collection of information. Send comments regarding this burden estimate or any other aspect of this collection of information, including suggestions for reducing this burden to Department of Defense, Washington Headquarters Services, Directorate for Information Operations and Reports (0704-0188), 1215 Jefferson Davis Highway, Suite 1204, Arlington, VA 22202-4302. Respondents should be aware that notwithstanding any other provision of law, no person shall be subject to any penalty for failing to comply with a collection of information if it does not display a currently valid OMB control number. PLEASE DO NOT RETURN YOUR FORM TO THE ABOVE ADDRESS.					
1. REPORT DATE (DD-MM-YYYY) 05-10-2013		2. REPORT TYPE		3. DATES COVERED (From - To)	
4. TITLE AND SUBTITLE Structural Changes and Convective Processes in Tropical Cyclones as Seen in Infrared and Water Vapor Satellite Data				5a. CONTRACT NUMBER	
				5b. GRANT NUMBER	
				5c. PROGRAM ELEMENT NUMBER	
6. AUTHOR(S) Fine, Caitlin Marie				5d. PROJECT NUMBER	
				5e. TASK NUMBER	
				5f. WORK UNIT NUMBER	
7. PERFORMING ORGANIZATION NAME(S) AND ADDRESS(ES)				8. PERFORMING ORGANIZATION REPORT NUMBER	
9. SPONSORING / MONITORING AGENCY NAME(S) AND ADDRESS(ES) U.S. Naval Academy Annapolis, MD 21402				10. SPONSOR/MONITOR'S ACRONYM(S)	
				11. SPONSOR/MONITOR'S REPORT NUMBER(S) Trident Scholar Report no. 413 (2013)	
12. DISTRIBUTION / AVAILABILITY STATEMENT This document has been approved for public release; its distribution is UNLIMITED.					
13. SUPPLEMENTARY NOTES					
14. ABSTRACT In the western North Pacific Ocean, tropical cyclone (TC) hazards, including strong winds, storm surge, high waves, and heavy rainfall, threaten archipelagos, densely crowded coastlines, and naval forces ashore and afloat. To accurately forecast TC track and intensity, meteorologists at the Joint Typhoon Warning Center (JTWC) must start from a thorough understanding of the TC's current structure. To accomplish this mission, they rely heavily upon satellite observations, particularly measurements in the water vapor (WV) and infrared (IR) channels on geostationary satellites. Therefore, it is critical to develop products that identify key TC structures in geostationary satellite data and track them over time, as these data are often the only real-time information available to the forecasters. This project examined satellite brightness temperatures in the WV and IR channels in 5 typhoon-strength TCs during the 2012 season to first identify the eye, eyewall, and regions of deep convection, and then to investigate the evolution of those features over time. The eye was defined in this study from the storm center out to the location of the minimum second derivative of IR brightness temperatures. The eyewall, which contains the strongest winds and deepest convective clouds, was divided into lower, middle, and upper sections using IR and WV brightness temperatures. The IR brightness temperatures in the upper eyewall and the eyewall slope, particularly in the region of the steep IR Tb gradient that included the lower eyewall, were found to be moderately negatively correlated to TC intensity.					
15. SUBJECT TERMS Typhoon, tropical cyclone, intensity, satellite, convection, eyewall					
16. SECURITY CLASSIFICATION OF:			17. LIMITATION OF ABSTRACT	18. NUMBER OF PAGES 33	19a. NAME OF RESPONSIBLE PERSON
a. REPORT	b. ABSTRACT	c. THIS PAGE			19b. TELEPHONE NUMBER (include area code)

U.S.N.A. --- Trident Scholar project report; no. 413

**Structural Changes and Convective Processes in Tropical Cyclones as Seen in Infrared and
Water Vapor Satellite Data**

By

**Midshipman 1/C Caitlin M. Fine
United States Naval Academy
Annapolis, Maryland**

(signature)

Certification of Advisers' Approval

**CDR Elizabeth R. Sanabia, Ph.D., USN, Permanent Military Professor
Oceanography Department**

(signature)

(date)

**Assistant Professor Bradford S. Barrett, Ph.D.
Oceanography Department**

(signature)

(date)

Acceptance for the Trident Scholar Committee

**Professor Maria J. Schroeder
Associate Director of Midshipman Research**

(signature)

(date)

USNA-1531-2

ABSTRACT

In the western North Pacific Ocean, tropical cyclone (TC) hazards, including strong winds, storm surge, high waves, and heavy rainfall, threaten archipelagos, densely crowded coastlines, and naval forces ashore and afloat. To accurately forecast TC track and intensity, meteorologists at the Joint Typhoon Warning Center (JTWC) must start from a thorough understanding of the TC's current structure. To accomplish this mission, they rely heavily upon satellite observations, particularly measurements in the water vapor (WV) and infrared (IR) channels on geostationary satellites. Therefore, it is critical to develop products that identify key TC structures in geostationary satellite data and track them over time, as these data are often the only real-time information available to the forecasters.

This project examined satellite brightness temperatures in the WV and IR channels in 5 typhoon-strength TCs during the 2012 season to first identify the eye, eyewall, and regions of deep convection, and then to investigate the evolution of those features over time. The eye was defined in this study from the storm center out to the location of the minimum second derivative of IR brightness temperatures. The eyewall, which contains the strongest winds and deepest convective clouds, was divided into lower, middle, and upper sections using IR and WV brightness temperatures. Eyewall slope was calculated between the break points of the eyewall using brightness temperatures and radial distance. The IR brightness temperatures in the upper eyewall were found to be moderately negatively correlated to TC intensity. Eyewall slope, particularly in the region of the steep IR Tb gradient that included the lower eyewall, was also found to be moderately negatively correlated to TC intensity.

Keywords: Typhoon, tropical cyclone, intensity, satellite, convection, eyewall

ACKNOWLEDGEMENTS

The author thanks Jeffrey Hawkins of the Marine Meteorology Division at the Naval Research Laboratory, Monterey, CA for providing geostationary satellite data and continued support, Chris Velden of the Cooperative Institute for Meteorological Satellite Studies at the University of Wisconsin, Madison for the use of the Automated Rotational Center Hurricane Eye Retrieval (ARCHER) method, and Dr. David Smith of the United States Naval Academy's Oceanography Department for his time and experienced guidance. The author also thanks the Trident Scholar committee members at the United States Naval Academy for their time and insight.

TABLE OF CONTENTS

ABSTRACT	1
ACKNOWLEDGEMENTS	2
TABLE OF CONTENTS	3
INTRODUCTION	4
DATA AND METHODS	14
RESULTS	22
CONCLUSIONS AND FUTURE RESEARCH	28
APPENDIX	30
REFERENCES	48

1. Introduction

a) Tropical Cyclone Structure

Tropical cyclones are low pressure systems with closed circulations that can feature heavy precipitation and strong winds (Riehl 1948). Tropical cyclones are composed of a primary and secondary circulation (Frank 1977). The primary circulation is defined as the tangential wind around a low pressure center and is counter-clockwise in the northern hemisphere and clockwise in the southern hemisphere (Frank 1977). The maximum tangential wind, and thus the strongest point of the primary circulation, is typically found in the eyewall (Frank 1977). The maximum tangential wind is what forecasters use to report tropical cyclone intensity. The secondary circulation is defined as an “in-up-out” flow of air parcels that results in cloud formation, and is important when examining tropical cyclone structure because it is the primary driver of convective development (Didlake and Houze 2012). The secondary circulation is vertically oriented and begins with air parcels moving radially inward at low levels (the “in” branch) from the environment outside the system to inside the TC circulation (Didlake and Houze 2012). While moving inward towards the TC center, parcels absorb sensible heat from the ocean, become more buoyant, and rise (the “up” branch) (Didlake and Houze 2012). During ascent, water vapor in the parcels condenses, forming clouds that comprise the most intense part of TC, the eyewall, and the less intense rainbands that spiral around a tropical cyclone (Didlake and Houze 2012). Convection in the eyewall can be so strong that cloud tops extend into the stratosphere, a condition known as “overshooting tops” (Olander and Velden 2009). During the ascent, water vapor in the air parcels condenses and releases latent heat of condensation, enhancing updrafts by accelerating upward motion (Houze 2010). Upon reaching the tropopause, which separates the troposphere from the stratosphere, the air parcels then diverge aloft and flow

radially outward (the “out” branch) (Didlake and Houze 2012). A negative secondary circulation, also known as subsidence, suppresses convection. This subsidence, as well as a temperature inversion that prevents moist air from rising much above the sea surface, inhibit cloud development in the eye (Houze et al. 2007). The strengthening or decay of the primary and secondary circulations are major internal contributors to intensity and structural changes, respectively, in tropical cyclones (Willoughby et al. 1982).

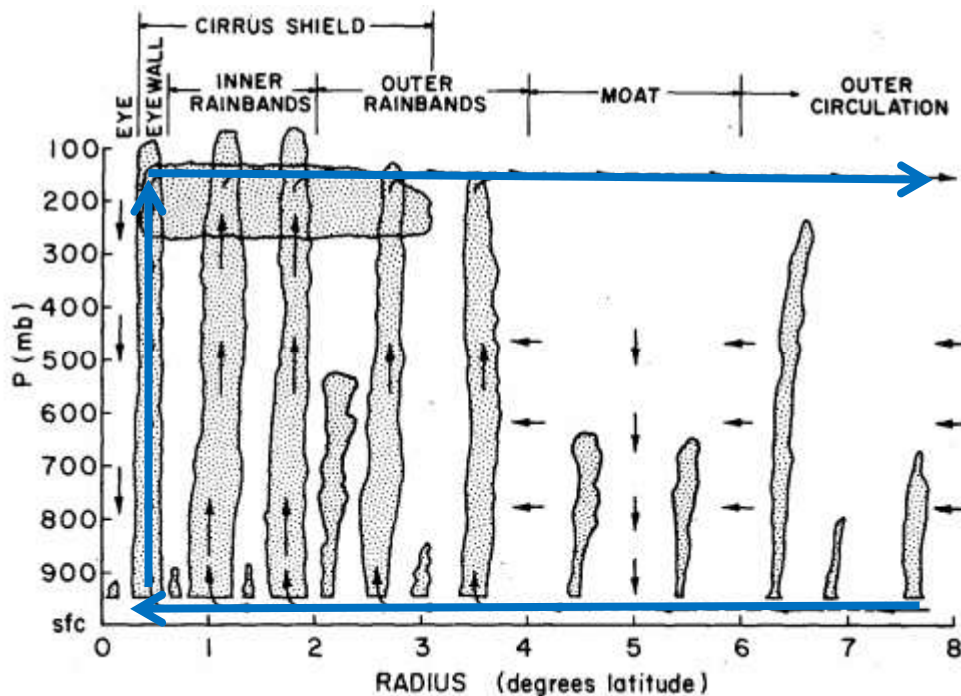


Figure 1. A vertical cross-section of a typical tropical cyclone. The arrows represent the predominant circulation, and the blue arrows highlight the secondary circulation. Near the surface, arrows denote the “in” branch of the secondary circulation. In each rainband and the eyewall, arrows show the “up” branch of the secondary circulation. Aloft, arrows symbolize the “out” portion of the secondary circulation. Overshooting tops are visible in the eyewall and inner rainbands (adapted from Frank 1977).

Two of the structural features identified and analyzed in this study are the TC eye and eyewall. The tropical cyclone eye is the location of the minimum sea level pressure in a TC, and is the center of primary circulation. The radius of the eye varies over time as the TC undergoes internal processes, such as eyewall replacement, or encounters adverse environmental conditions,

but usually ranges between 5-50 km (Frank 1977). The eyewall, the location of the tallest clouds in the TC, surrounds the eye (Frank 1977). Except in cases of eyewall replacement, the eyewall features the deepest convection (and by extension, the strongest secondary circulation), in the TC (Houze et al. 2007). Between the eye and the tallest clouds in the eyewall, cloud height slopes outwards; observers flying through a TC eye report seeing the “stadium effect”, where the eye is analogous to a playing field and the eyewall is likened to the tiers of seats surrounding the field (Hazelton and Hart 2013). Eyewall slope is defined in Hazelton and Hart (2013) as the departure of the eyewall from the vertical. Smaller eyewall slope, indicating a more upright eye and steeper transition from the eye to the eyewall, has been linked to greater TC intensity (Kossin et al. 2007, Hazelton and Hart 2013). This study explores the connections between the characteristics and evolution of the TC eye and eyewall structure to intensity by tracking the eye and eyewall over time in Hovmöller diagrams of infrared (IR) imagery and deep convection.

b) *Tropical Cyclone Intensity*

Tropical cyclone intensity, usually reported as the instantaneous maximum surface wind speed, is a measure of the strength of the primary circulation (Frank 1977). Tropical cyclones are categorized by their intensity: a tropical depression has 1-minute sustained winds less than 34 knots; a tropical storm, greater than or equal to 34 and less than 64 knots; a typhoon, greater than or equal to 64 knots; and a super typhoon, greater than or equal to 130 knots (JTWC).

Though all TCs in this study exceeded typhoon strength, it is helpful to examine the conditions that foster TC formation and encourage TC growth. Six necessary but not sufficient conditions for TC formation are: 1) the sea surface temperature must exceed 26.5°C, as is the case in most tropical seas for over half of the year, 2) latitude must be at least 5° North or South of the equator so the requisite amount of Coriolis force is present, 3) vertical wind shear must be

low, or the disturbance will have its cloud tops shorn off and dissipate, 4) vorticity must be high, to provide the necessary spin, 5) conditional instability, which enables thunderstorm activity, must be present, and 6) mid-tropospheric air must be humid (Gray 1968). Changes in one or more of these environmental conditions can result in the strengthening or weakening of an existing TC.

Once a tropical depression has formed and intensified into a tropical storm, the maturing tropical storm will often develop a central dense overcast (CDO) layer of cirrus clouds that obscures all structural features in IR satellite imagery (Frank 1977). A tropical cyclone may undergo episodes of rapid intensification, usually in conjunction with re-organization of its structure, such as when transitioning from tropical storm to a typhoon (Houze 2010). Greater intensity usually implies greater damage potential. However, the width of a TC may also lead to more damage; a broader wind field, or “fetch”, generates a higher storm surge than would a smaller storm of the same intensity when landfall is imminent (Kossin and Sitkowski 2008). Knowledge of these types of structural properties in TCs is critically important to the warning process.

Sometimes, after exceeding typhoon strength intensity, TCs may develop secondary eyewalls and experience an eyewall replacement cycle (ERC), in which the secondary eyewall disrupts inflow into the primary eyewall, the primary eyewall dissipates, and the former secondary eyewall contracts inwards towards the storm center (Kossin and Sitkowski 2008). Kuo et al. (2009) noted that 40% of intense (Saffir-Simpson Category 4 or higher) Atlantic hurricanes, 60% of Eastern Pacific hurricanes, and 80% of Western Pacific typhoons sampled exhibited secondary eyewalls at some point in their lifecycle. While maximum wind speed decreases during an ERC, which may last several days, tangential wind speeds and the radius of

maximum winds frequently increase afterwards, enlarging the fetch area and leading to a higher storm surge (Kossin and Sitkowski 2008).

In the final stage of the TC lifecycle, tropical cyclones dissipate; common causes include the TC moving into colder water, encountering areas of high wind shear, or making landfall (Houze 2010). If a TC travels into the mid-latitudes, it may undergo extratropical transition, and become an extratropical cyclone (Jones et al. 2003). This study aims to identify and track structural features in TCs, and to connect TC structure to intensity throughout the TC lifecycle. There are various methods that meteorologists use to diagnose current TC structure and to link TC structure to intensity, several of which are discussed below.

c) *Objective Methods for Determining TC Structure and Intensity Using IR Satellite Data*

The Dvorak technique is a widely used method by which to estimate the intensity of a TC using satellite data. The Dvorak technique involves the interpretation of several types of satellite data, including infrared and visible data, to determine TC intensity (Dvorak 1984). To use the Dvorak technique, forecasters must first identify the TC eye or Low-Level Circulation Center (LLCC) (Dvorak 1975). Forecasters then assign the TC a T-number according to which characteristics the TC exhibits, such as a CDO (Dvorak 1975). Each T-number corresponds to a range of possible intensities determined by historical compilation of storm intensities of TCs displaying those specific structural features (Dvorak 1975). In the advanced Dvorak technique (ADT), the most current version of the Dvorak technique, the average IR brightness temperature is computed within different ranges, varying from 25-125 km radially outward from the TC center (Velden et al. 2006). The Dvorak technique then uses the coldest Tb radius and value in the eyewall, and the warmest Tb radius and value in the eye, to determine an estimate of TC intensity (Velden et al. 2006).

Biases, determined by comparing Dvorak technique estimates to aircraft reconnaissance data sourced from the databases of the Automated Tropical Cyclone Forecasting (ATCF) system, include underestimating intensities for each of the following types of TCs: developing tropical storms with maximum velocities between 35 and 55 knots, intense typhoons with maximum wind speeds exceeding 125 knots, and intensifying, high-latitude, or slow-moving TCs (Knaff et al. 2010). The technique also overestimates intensities for moderate typhoons with maximum velocities between 75 and 125 knots and weakening or fast-moving TCs (Knaff et al. 2010). The Advanced Dvorak Technique (ADT), an updated version of the Dvorak technique, mitigates some of these biases by performing additional analysis on geostationary satellite data. The ADT incorporates and automates center-finding and enhanced pattern-recognition algorithms using gradients in IR data, thus improving upon the accuracy of the Dvorak technique for tropical storm and depression-strength systems, high-latitude systems, and TCs with pinhole eyes (Olander and Velden 2007). While the accuracy of the Dvorak technique has improved over time, and it remains generally internally consistent between different agencies and forecasters, intensity estimates from other methods that utilize satellite data can vary widely, as shown in satellite consensus techniques that analyze different intensity estimates (e.g. SATCON) (Herndon and Velden 2007), thus indicating the need to further investigate other methods of manipulating IR data to determine TC structure and its connections to and impacts on TC intensity.

Kossin et al. (2007) devised another method that utilized different types of satellite data to diagnose an element of TC structure and connect it to intensity. Measuring the eye size in IR data where the eye was clearly visible, Kossin et al. (2007) estimated the radius of maximum winds (RMW), as well as the radii of the 34-knot, 50-knot, and 64-knot winds. Historical

measurements of RMW made with reconnaissance aircraft were regressed onto IR eye sizes, yielding a strong linear relationship (Kossin et al. 2007). This RMW was then incorporated into an algorithm that analyzes Advanced Microwave Sounding Unit (AMSU) microwave data to determine intensity (Kossin et al. 2007). The IR-derived RMW reduced the error in the AMSU intensity estimation method by 30%, as compared to intensity estimates that used the RMW found in the Automated Tropical Cyclone Forecast (ATCF) system databases (Kossin et al. 2007). However, AMSU, like all other microwave imagers, is mounted on a polar-orbiting satellite, and thus only makes two passes over any given TC a day (Brueske and Velden 2003). Furthermore, its 48-km resolution, already coarse, worsens with distance from the nadir of the swath, so accuracy of this technique varies by image, depending on the location of the TC within the scan (Brueske and Velden 2003). While the less-than-ideal spatial and temporal resolution of the AMSU satellite hinders its utility as a stand-alone intensity estimation method, this technique does demonstrate the ability to detect structural features in infrared satellite data and relate them to intensity.

Additionally, Kossin et al. (2007) determined through IR Tb analysis that a coincident warmer TC eye and a colder TC eyewall were well correlated to TC intensity. The Dvorak technique also compares the warmest brightness temperature in the eye to the coldest brightness temperature in the eyewall (Velden et al. 2006). Kossin et al. (2007) agreed with the findings in Dvorak (1984), which stated that a greater Tb difference between the eye and eyewall was usually associated with higher intensity.

Another method that related TC structure and intensity quantified the symmetry of a TC to make intensity estimates, under the hypothesis that less symmetric storms are less intense than more symmetric, or annular, storms with the same characteristics (Piñeros et al. 2011).

Brightness temperature gradients in IR satellite data from the examined TCs were compared to those in an ideal, completely symmetric vortex (Piñeros et al. 2011). This technique demonstrated a connection between TC structure, evidence of the secondary circulation, and TC intensity, a measure of the primary circulation.

d) Brightness Temperature Differencing

Water vapor minus infrared (WV-IR) brightness temperature differencing is another method of using satellite data to identify important TC structural features. In WV-IR brightness temperature differencing, infrared brightness temperatures are subtracted from water vapor brightness temperatures. Satellites measure radiance of IR wavelengths emitted from cloud tops, and radiance of WV wavelengths emitted from water vapor above the cloud tops. Fritz and Laszlo (1993) capitalized on this radiative property of tall clouds, first observing that the WV channel at 6.7 μm measured warmer brightness temperatures than the IR channel at 11.1 μm when clouds reached to the 200 millibar level, which is about the level of the tropopause. Due to the temperature inversion at the tropopause (separation of the troposphere from the stratosphere), a parcel above the tropopause that is higher in altitude is warmer than one of lower altitude at the same location, so a positive WV-IR T_b difference indicates overshooting tops (Olander and Velden 2009). Overshooting tops highlight the locations of strongest convection in the storm; therefore, positive brightness temperature differences can be used to reveal areas of deep convection, such as eyewalls, that are not apparent in the IR or WV imagery alone. For example, in the rightmost image in Figure 2, warmer colors represented larger brightness temperature differences, and therefore areas of overshooting tops and deeper convection. Brightness temperature differences revealed an eyewall and convective band not clearly visible in infrared imagery alone. In Olander and Velden (2009), brightness temperature differencing compared

favorably to microwave imagery in detecting bursts of deep convection embedded in a cirrus cloud canopy.

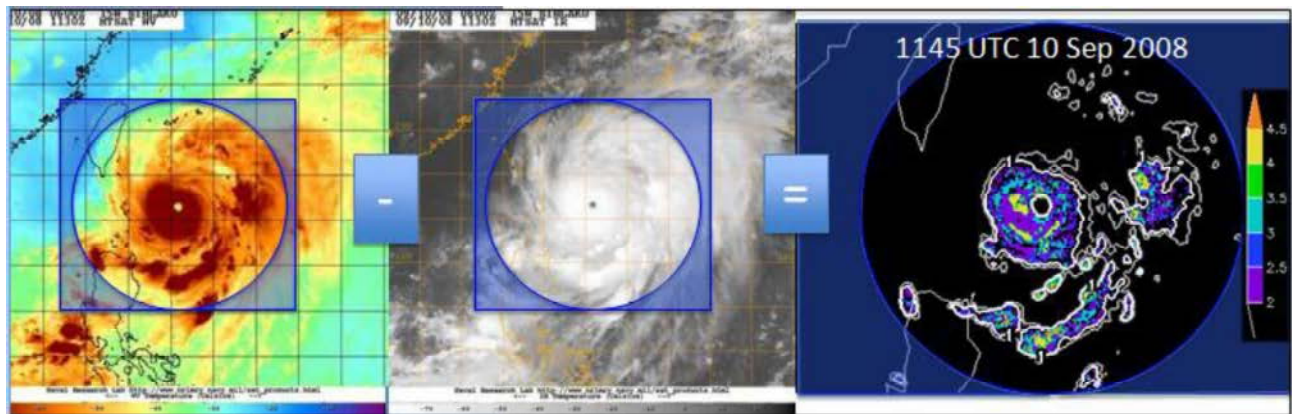


Figure 2: A graphical depiction of brightness temperature differencing. Leftmost image: water vapor imagery. Middle image: infrared imagery. Right image: positive brightness temperature differences. Image of Typhoon Sinlaku (2008) from Celone (2011).

The high temporal frequency of geostationary satellite images, in which one image is usually received every 30 minutes (though occasionally the interval between images may span several hours), combined with the ability of brightness temperature differencing to clearly show deep convection in TCs, enable the detailed analysis of structural changes in TCs over time.

Experimentally, high positive brightness temperature differences have been highly correlated with significant pressure decreases and intensity increases 24 hours later (Olander and Velden 2009). This indicates that Tb differencing may also be used to investigate intensity changes in tropical cyclones and has potential for predictive capability (Kossin and Sitkowski 2009).

e) Eyewall Slope

Hazelton and Hart (2013) investigated slope of eyewall clouds and concluded that a steeper eyewall slope is correlated to higher TC intensity. They identified reflectivity contours in radar data gathered onboard hurricane reconnaissance aircraft in the Atlantic basin and computed slope, which they physically interpreted as the outward slant of the eyewall cloud, measured by a departure from the vertical (Hazelton and Hart 2013). Eyewall slope was

averaged across 6-hour bins and compared to best-track intensity. Hazelton and Hart (2013) then found that a greater eyewall slope was linked to stronger TC intensity. This result suggests that observations from the TC inner core in particular are valuable for better understanding the connection between TC structure and intensity. Despite aircraft reflectivity data having a higher horizontal spatial resolution than that of geostationary satellite data, coverage of TCs by aircraft data is limited by the number of flights that are flown into a given TC, and by the maximum range of a reconnaissance aircraft (Kossin et al. 2007). Thus, a technique that can calculate slope from geostationary satellite data would be useful.

This current study uses IR brightness temperatures alone and WV-IR brightness temperature differences to identify two key inner-core structural features, the TC eye and eyewall, map their evolution over time, and investigate connections between TC structure and intensity. In particular, this study examines the relationship between brightness temperatures in the eyewall, eyewall slope, and TC intensity in five typhoons during ten weeks of the 2012 western North Pacific TC season. Section 2 describes the data and methods used in this study. Section 3 details the results produced by this method. Implications of the results are explored in Section 4. Lifecycle summaries of the five typhoons are included in the Appendix.

2. Data and Methods

a) Data

Five typhoons from a ten week period during the 2012 western North Pacific typhoon season were analyzed: Typhoons Sanba, Bolaven, Jelawat, Prapiroon, and Son-Tinh. Maximum tangential wind speeds in each typhoon exceeded 100 knots, and each typhoon featured a visible eye at some point during its lifetime (Table 1). A total of 821 unique times with both infrared and water vapor satellite measurements available were examined. Since this study focused on structural and intensity changes in the selected TCs, an understanding of the critical events in their lifecycles is beneficial. Summaries of each TC's lifecycle are provided in the appendix.

Table 1. Minimum sea level pressure, maximum tangential wind speed, number of days the TC was at or above typhoon (TY) intensity, and number of data points during periods when the TCs featured visually identifiable eyes.

Typhoon	Min pressure (mb)	Max wind speed (kts)	Days above TY intensity	Datapoints with visually identifiable eyes
Bolaven	929	125	6.25	97
Sanba	911	150	4.75	186
Jelawat	918	140	7.25	299
Prapiroon	948	100	7	200
Son-Tinh	941	110	2	39
			Total:	821

The satellite data used in this study came from the Multi-function Transport Satellite (MTSAT)-2, a geostationary satellite operated by the Japan Meteorological Agency (JMA). Geostationary satellite sensors measure electromagnetic radiation at visible, infrared, and water vapor wavelengths. Each geostationary satellite has multiple channels. Channel 1 on MTSAT-2 measures radiance of IR wavelengths between 10.3-12.5 μm . Channel 3 on MTSAT-2 measures radiance of WV wavelengths between 6.5-7 μm . The horizontal resolution for the IR and WV channels is 4 km (CEOS 2012). The Marine Meteorology Division at the Naval Research Laboratory (NRL), Monterey, California, uses TeraScan, a software system built for data and

image manipulation, to automatically apply satellite corrections to data and to create the satellite imagery products available on their public webpage (NESDIS 2012). The digital brightness temperature data used in this study came directly from the NRL automated and corrected TeraScan output. The typhoon intensities used in this study were taken from Joint Typhoon Warning Center (JTWC) warning products. Every 6 hours, JTWC issues warning positions with center latitude, longitude, and intensity estimates.

b) *Methodology*

The success of this brightness temperature analysis and differencing technique depended largely upon the accuracy of the TC center location. When the TC eyes were clear in IR imagery, they were visually identified in plotted IR data to an accuracy of 0.025° , which is approximately one satellite pixel at this horizontal resolution. Once the storm center's latitude and longitude were determined, they were subtracted from the native IR or WV latitude and longitude. This step served to storm-center the data; instead of the data array being defined in native longitude and latitude coordinates, as it was previously, coordinates were defined as distances in radial degrees from the center location, and ranged from -5.5° to 5.5° from the storm center.

The storm-centered infrared and water vapor satellite data were then transformed from a Cartesian grid onto a polar grid. Infrared brightness temperatures in this new, transformed coordinate system were subtracted from water vapor brightness temperatures in the new, transformed grid to calculate WV-IR Tb differences. For every timestep, either positive WV-IR Tb differences or IR Tb differences alone were azimuthally averaged at points spaced every 1° around a radial, and the averaging repeated for all radials from 0.02-5.5 radial degrees at 0.02° intervals, after Celone (2011) (Fig. 3). If the location of the TC center was incorrectly identified, the radial range rings would not be equidistant from the actual TC eye at all points on the ring,

and thus the azimuthal averaging technique would not accurately capture the structure of the TC. The positive Tb difference averages and IR Tb averages produced by this method were plotted on Hovmöller graphs (Figs. 3 (right), 4) that display the radial variation in deep convection and cloud top brightness temperature, respectively, on the x-axis over time.

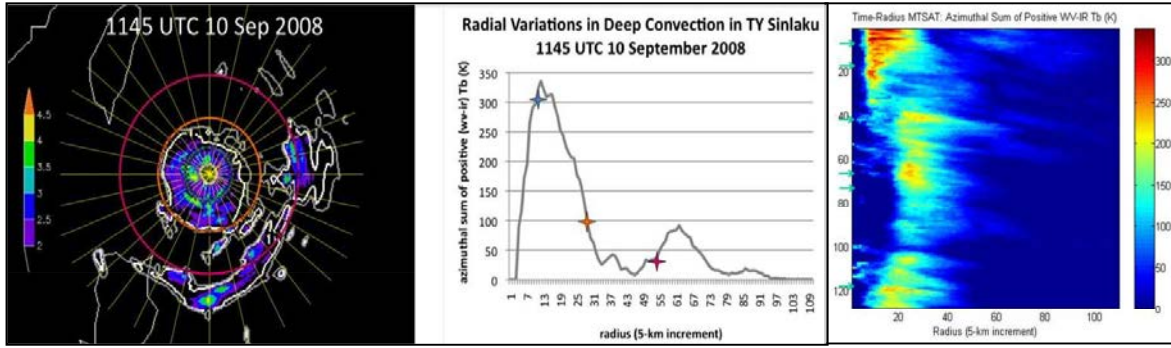


Figure 3: Left: Positive WV-IR Tb differences, showing radii around which positive WV-IR Tb differences are averaged at the azimuths, not to scale, for demonstrative purposes. Middle: Radial profile of averaged positive WV-IR differences. Right: Radial variation of positive WV-IR difference averages over time (from Celone 2011).

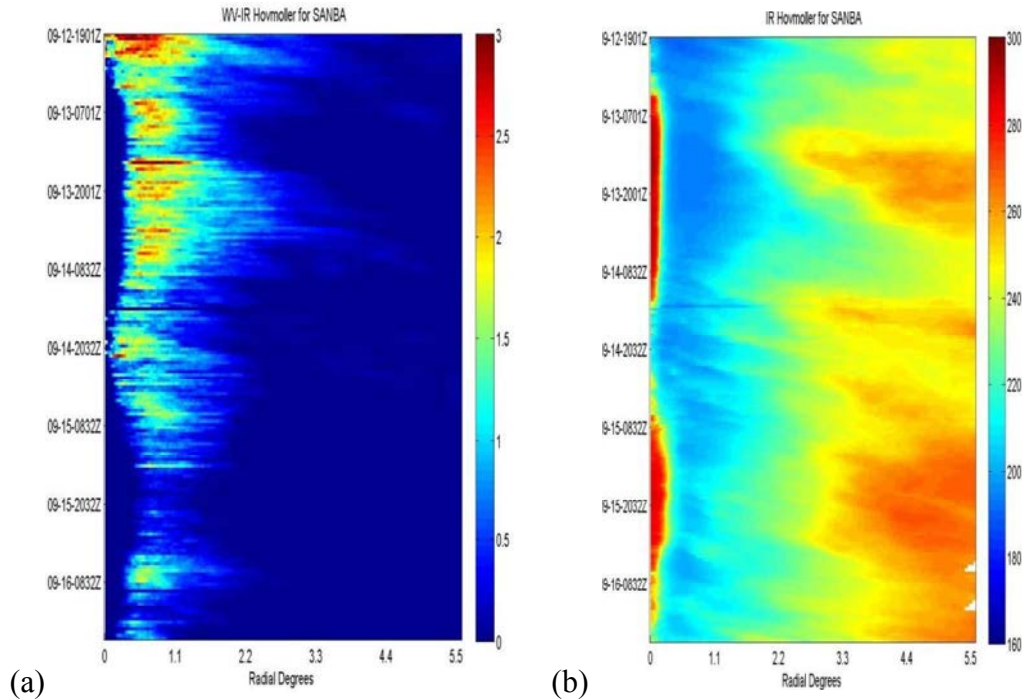


Figure 4. a) Radial variation (x-axis) of a) deep convection (positive WV-IR difference averages) and b) cloud top temperatures (IR Tb averages) over time (y-axis).

Based in part on subjective analysis of the Hovmöller diagrams for each TC, the eyewall was divided into three sections: lower, middle, and upper (Fig. 5). Using the brightness

temperature averages plotted on the Hovmöller diagrams, three points were identified that delineated the eyewall sections. The start of the middle eyewall (point “B” in Fig. 5), which was intended to show the inner edge of the eyewall, was objectively defined as the maximum of the second derivative (Laplacian) of IR Tb averages. Another point, the start of the lower eyewall (point “A” in Fig. 5) was introduced and defined as the minimum of the Laplacian of IR Tb averages. It is important to note that, despite the objectivity of this definition, the point marking of the start of the middle eyewall was not always physically realistic. For example, in 6.1% of the cases, the point marking the start of the middle eyewall was warmer than the point marking the start of the lower eyewall, meaning the middle of the eyewall was located lower in the atmosphere than the start of the eyewall. The start of the middle eyewall, which should be located higher in the atmosphere, should have been cooler. Possible reasons for the technique not performing as expected for these cases include (1) incorrect identification of the TC center, (2) significant asymmetry in the TC, and (3) a complex pattern of inner-core convection. The start of the upper eyewall, which denoted the most radially inward location of overshooting tops for that time, was objectively defined as the first positive WV-IR Tb difference. Though the radius of the start of the upper eyewall was found using WV-IR difference averages, this study used the IR Tb average value at that radius for calculations. For reasons which may be similar to problems with the start of the middle eyewall, the start of the upper eyewall occurred radially inward of the start of the middle eyewall in 11.8% of cases. Finally, the limit of the upper eyewall, which represented the coldest cloud top temperature at the time, was objectively defined as the minimum IR Tb average. The evolution of the four identified points during the lifecycle of Super Typhoon Sanba can be seen via the Hovmöllers of IR Tb averages, or WV-IR Tb difference averages (Fig. 6).

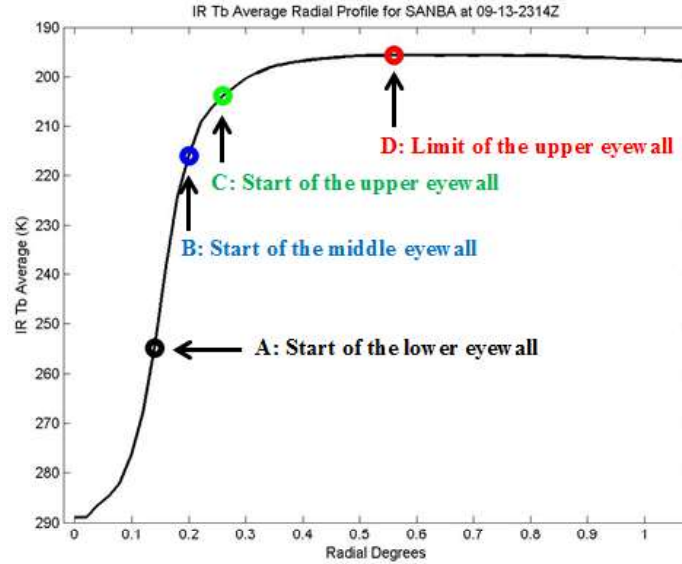


Figure 5. Radial cross-section of IR brightness temperature averages in Super Typhoon Sanba at 2314 UTC 13 September 2012. A: the minimum of the IR Laplacian function, B: the maximum of the IR Laplacian function, C: the first positive WV-IR difference, and D: the minimum IR Tb average value.

Once the four inner-core structural points were defined and the eyewall sections delineated, eyewall slope between structural features was calculated using the IR brightness temperatures (in K) at each feature and the radial distance (in degrees) between the radii of the two structural features from the center. Four eyewall slopes were analyzed: lower, mid-lower, upper-lower, and middle (Fig. 7), all with units of K deg^{-1} .

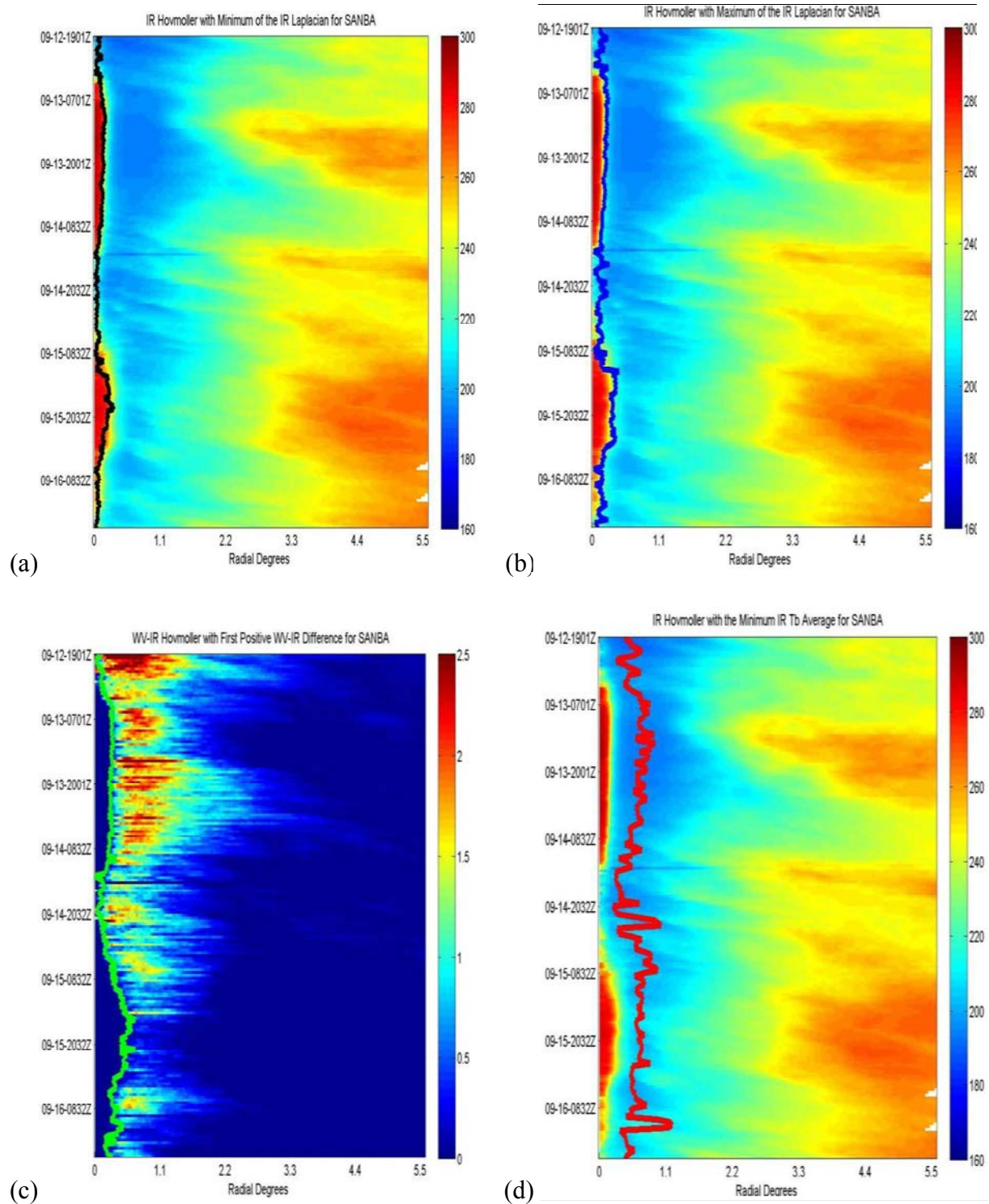


Figure 6. Start of the a) lower, and b) middle eyewall, and d) limit of the upper eyewall, superimposed on the radial variation of average brightness temperatures over time. c) Start of the upper eyewall superimposed on the radial variation of average brightness temperature differences over time.

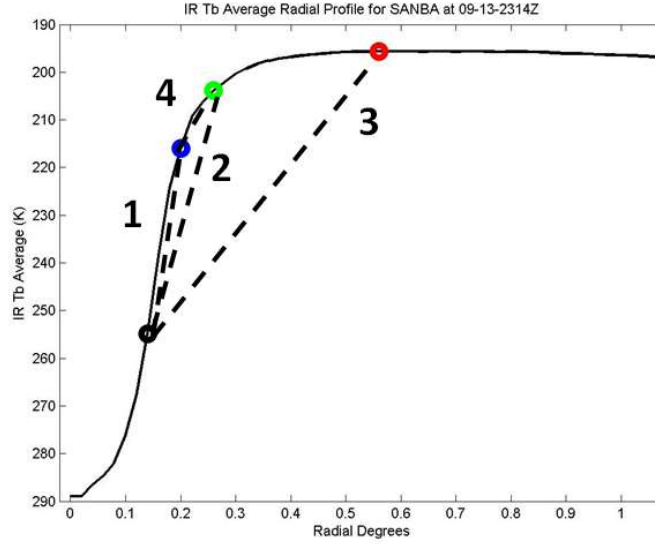


Figure 7: Radial cross-section of IR brightness temperature averages in Super Typhoon Sanba at 2314 UTC 13 September 2012. Dashed lines indicate eyewall slopes for the 1) lower, 2) mid-lower, 3) upper-lower, and 4) middle eyewall.

The equations for the four eyewall slopes are as follows:

$$\text{Lower eyewall slope} = \frac{T_{b\text{blue}} - T_{b\text{black}}}{R_{b\text{blue}} - R_{b\text{black}}} \quad (1)$$

$$\text{Mid-lower eyewall slope} = \frac{T_{b\text{green}} - T_{b\text{black}}}{R_{g\text{green}} - R_{b\text{black}}} \quad (2)$$

$$\text{Upper-lower eyewall slope} = \frac{T_{b\text{red}} - T_{b\text{black}}}{R_{r\text{red}} - R_{b\text{black}}} \quad (3)$$

$$\text{Middle eyewall slope} = \frac{T_{b\text{green}} - T_{b\text{blue}}}{R_{g\text{green}} - R_{b\text{blue}}} \quad (4)$$

To quantify the relationship between eyewall slope and TC intensity, quadratic best-fit lines were calculated for each of the eyewall slopes vs. 6-hourly JTWC intensity. The co-efficient of determination, R^2 , was determined for the best fit line, and root-mean square error (RMSE) was calculated using the formula:

$$RMSE = \sqrt{\frac{\sum_{t=1}^n (y_t - \hat{y}_t)^2}{n}},$$

where y_t is the actual value of the dependent variable (in this case, eyewall slope), \hat{y}_t is the value of the dependent variable (eyewall slope) computed using the best-fit line equation, and n is the sample size. A flowchart describing the input, method, and output of both the WV-IR brightness

temperature differencing and the IR brightness temperature analysis techniques used in the identification of the inner-core structural features and calculation of eyewall slope is shown in

Figure 8.

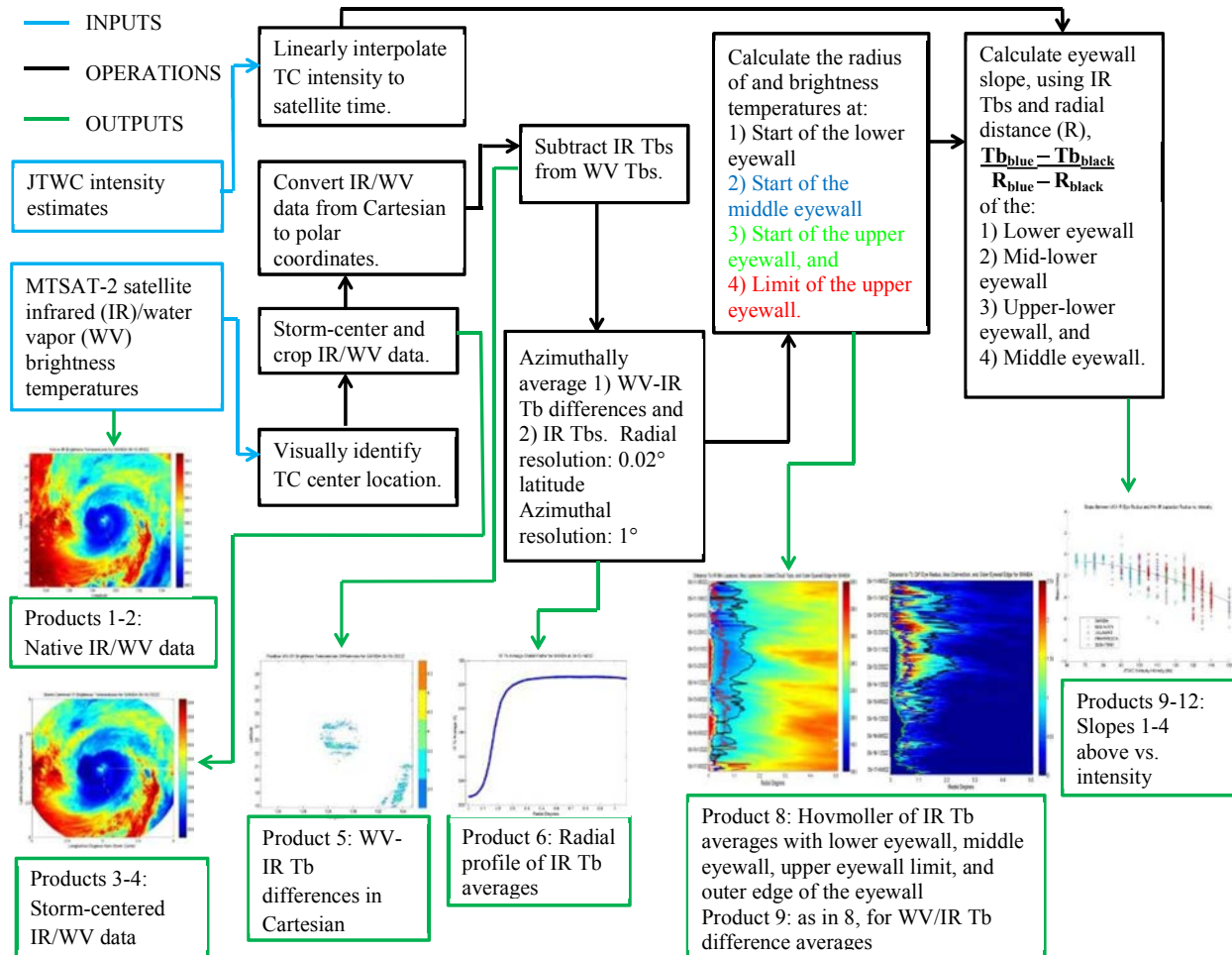


Figure 8: The Deep Convection Tracker: data, operations, and products.

3. Results

a) Eyewall Cloud Brightness Temperature

Comparing IR Tb averages at the start and limit of the upper eyewall to TC intensity yielded a consistent negative relationship between IR brightness temperature and TC intensity. Lower IR brightness temperatures were observed at the upper eyewall points during periods of increased TC intensity (Figs. 9a,b), physically signifying that taller clouds in the eyewall were linked to stronger TC intensity. However, the IR brightness temperatures at the starts of the lower and middle eyewalls did not demonstrate a consistent relationship between IR brightness temperature and TC intensity (Figs. 9c,d).

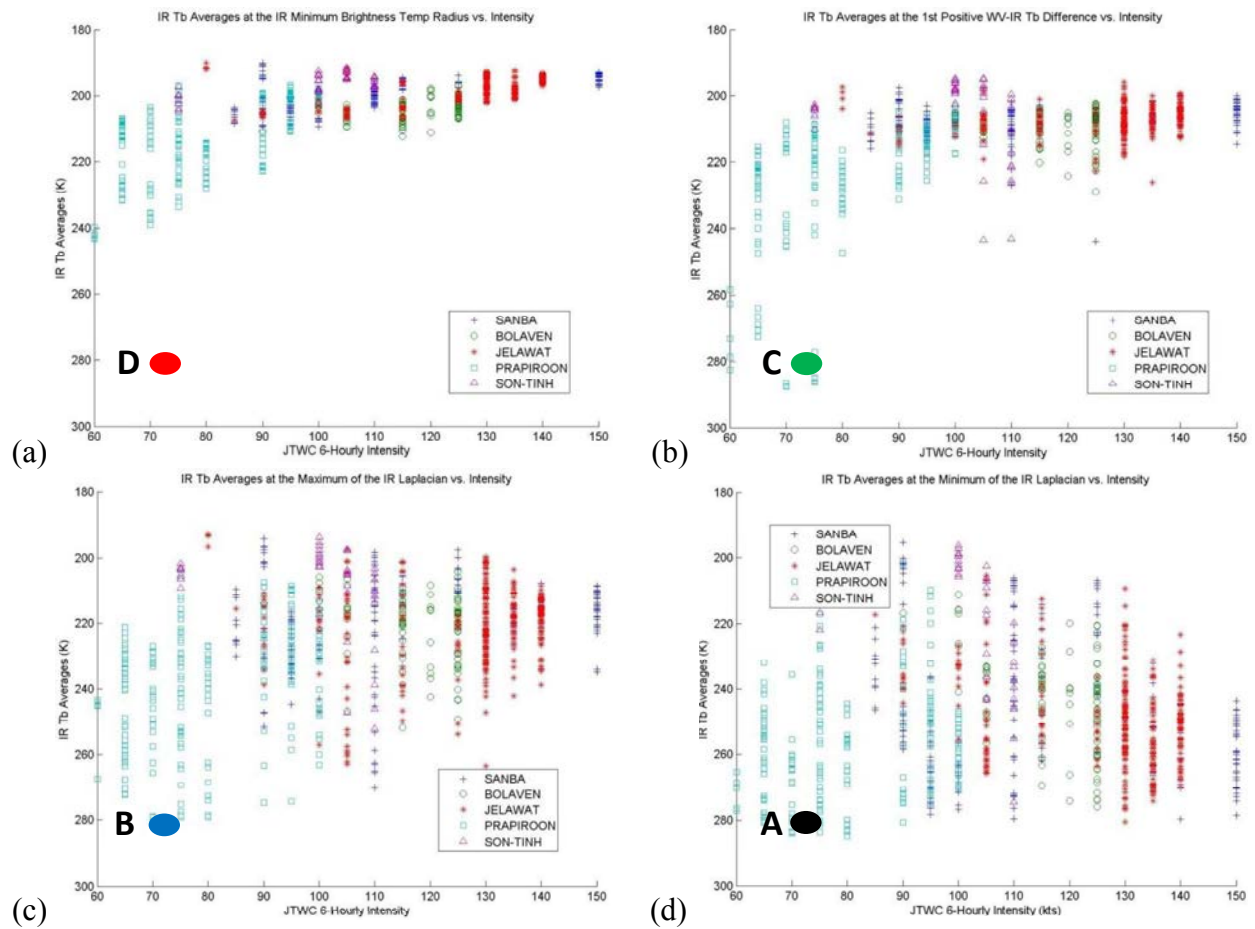


Figure 9. Infrared Tb averages (K) vs. intensity (kts) at the A) limit of the upper eyewall and at the start of the B) upper eyewall, C) middle eyewall, and D) lower eyewall.

At the limit of the upper eyewall (point “D” in Fig. 5), the warmest IR Tb averages occurred at the lowest intensities, just above typhoon strength (Fig. 9a). The range of IR Tb averages decreased as TC intensity increased (Fig. 9a). At the highest intensities, between 140-150 knots, the Tb averages were confined to a small cluster below 200K, although it is worth noting that these intensities persisted for only a short period of time and were comprised of a smaller sample size compared to other intensities (Fig. 9a). Physically, lower IR Tbs represent higher cloud tops. As IR Tbs at the limit of the upper eyewall decreased, they were associated with a stronger primary circulation. That is, as cloud tops grew higher, the intensity of the storm increased as well.

At the start of the upper eyewall (point “C” in Fig. 5), as at the limit of the upper eyewall, the coldest IR Tb averages were associated with the most intense TCs (Fig. 9b). As TC intensity increased, while the lower bound of IR Tb averages remained roughly constant, the upper value of IR Tb averages for a given intensity decreased (Fig. 9b). At the limit of the upper eyewall, many IR Tb averages were below 200K, including those at the highest TC intensities. However, at the start of the upper eyewall, few IR Tb averages occurred below 200K (Fig. 9b). The limit of the upper eyewall should be colder than the start of the upper eyewall because lower IR brightness temperatures represent taller clouds. Lower infrared Tbs in the upper eyewall suggest that taller clouds corresponded to greater TC intensity. This agrees with Dvorak (1984), who linked colder IR Tbs in infrared satellite data to greater TC intensity, and made that finding one of the cornerstones of his intensity estimation technique.

Infrared Tb averages at the start of the middle eyewall (point “B” in Fig. 5) displayed no noticeable relationship to TC intensity (Fig. 9c). The range of IR Tbs was smaller when TC intensity was stronger, but that result may be due to the reduced sample size at higher intensities.

The mean of the IR Tb averages at the start of the middle eyewall was much warmer than that of the IR Tb averages in the upper eyewall. Physically, this means that cloud tops at the start of the middle eyewall were lower in height than cloud tops in the upper eyewall, which was expected, given the definition and distribution of the points (Fig. 5).

Infrared Tb averages at the start of the lower eyewall (point “A” in Fig. 5) also demonstrated no consistent relationship to TC intensity. The lack of relationship between intensity and the start of the lower and middle eyewalls demonstrates that the brightness temperatures of clouds in the lower portion of the eyewall, treated by themselves, would not be a very useful tool to determine current intensity from IR and WV satellite data. However, the apparent negative relationship between IR Tb averages at the start and limit of the upper eyewall and TC intensity indicates that the brightness temperatures of cold clouds in the upper eyewall may be used to estimate current TC intensity using satellite data, which is indeed the cornerstone of the widely utilized Dvorak technique.

b) Eyewall Slope

The lower eyewall and mid-lower eyewall slopes (dashed segments 1 and 2, respectively, in Fig. 7) demonstrated a strong negative relationship to intensity. More negative slope, indicating a larger difference between IR brightness temperature sums at the two compared points and/or a smaller radial separation between the points, corresponded to increased intensity (Figs. 10a,b). The upper eyewall and middle eyewall slopes (dashed segments 3 and 4, respectively, in Fig. 7) showed a poor relationship to intensity (Figs. 10c,d). To quantify the relationship between intensity and eyewall slope, a quadratic best-fit line, its co-efficient of determination (R^2), and root-mean square error (RMSE) were calculated for each eyewall slope (Table 2).

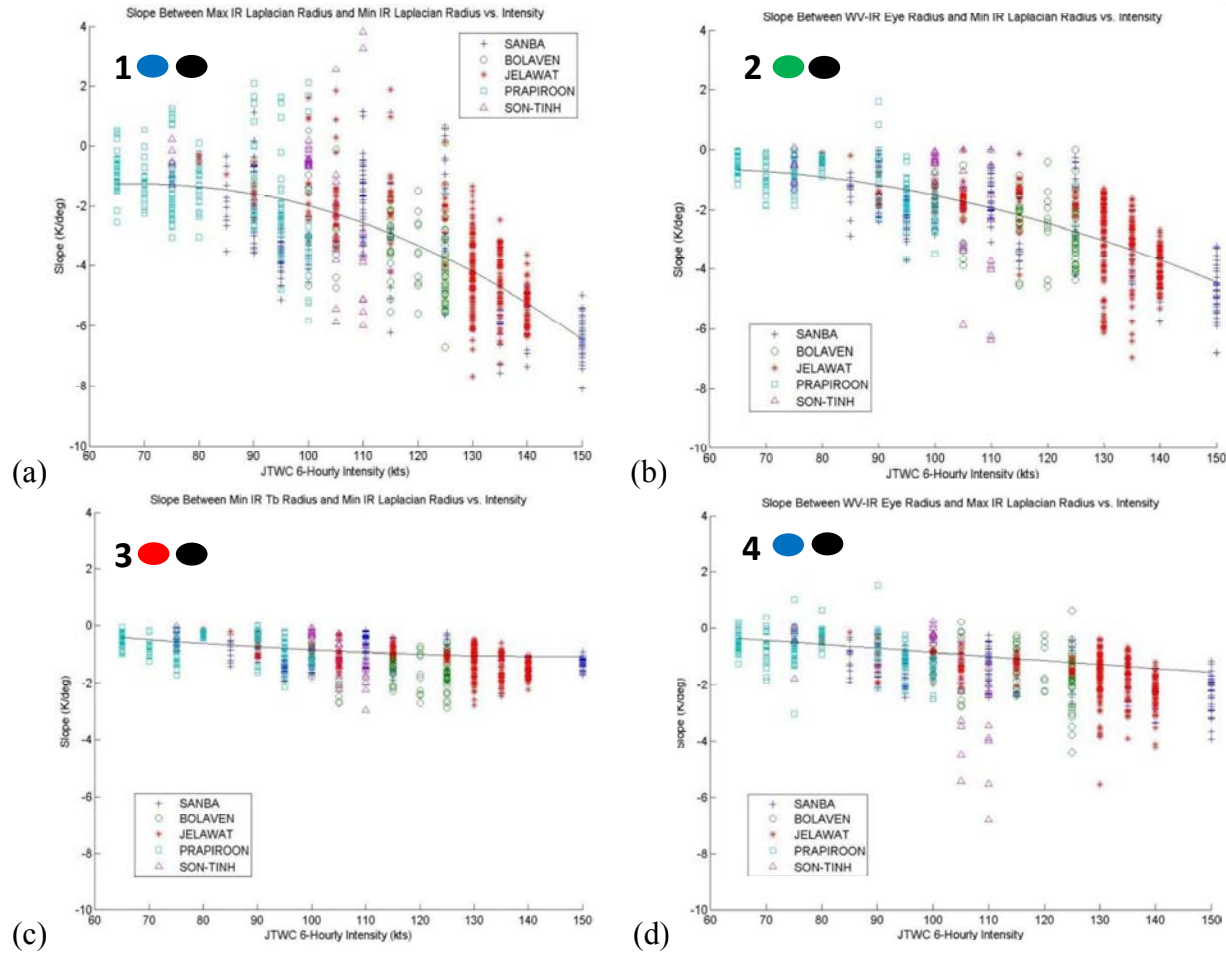


Figure 10. The eyewall slope ($K \text{ deg}^{-1}$) vs. intensity (kts) for the 1) lower, 2) mid-lower, 3) upper-lower, and 4) middle eyewall. The black line represents the quadratic best-fit line.

Table 2: R^2 and RMSE of the best-fit lines for eyewall slopes plotted against intensity from JTWC.

	R^2 of best-fit line	Root-mean square error ($K \text{ deg}^{-1}$)
Lower eyewall slope	0.52	2.57
Mid-lower eyewall slope	0.55	1.75
Upper-lower eyewall slope	0.23	0.87
Middle eyewall slope	0.24	1.47

Lower eyewall slope was found to have a negative relationship to TC intensity (Fig. 10a). By definition and design, the lower eyewall should have contained the steepest slope (Fig. 7). A more negative lower eyewall slope value indicated that the eyewall was more upright, which coincided with higher TC intensity (Fig. 10b). An R^2 value of 0.52 (Table 2) indicated TC

intensity and lower eyewall slope were moderately correlated (Wilks 1996). The large RMSE (2.57 K deg^{-1}) did not necessarily signal a poor relationship between TC intensity and lower eyewall slope; the spread of slopes at each intensity remained large until intensity reached 140 knots and greater, leading to a large RMSE (Table 2).

Mid-lower eyewall slope also demonstrated a negative relationship to TC intensity (Fig. 10b). The mean mid-lower eyewall slope had less magnitude than the mean of the lower eyewall slope in Fig. 7, which physically means that, for a given TC intensity, the lower eyewall cloud was more upright than the mid-lower eyewall cloud. The R^2 value of the best fit line for mid-lower eyewall slope (0.55) slightly exceeded that of the lower eyewall slope, likely due to the reduced spread overall of slope values for the mid-lower eyewall (Table 2). Lower RMSE (1.75 K deg^{-1}) reflects the smaller range of slope values in the mid-lower eyewall as well (Table 2). Like the lower eyewall slope, the mid-lower eyewall slope has a negative relationship between eyewall slope and TC intensity.

Upper-lower eyewall slope did not have a relationship to TC intensity (Fig. 10c). The slope, as measured from the upper to lower eyewalls, was consistently shallower than the slope between any other points. Though RMSE (0.87 K deg^{-1}) was low, it measured the spread between the best-fit line and paired slope-intensity observation. The small R^2 (0.23) corroborated the lack of statistically significant relationship (Table 2).

Middle eyewall slope also did not have a relationship to TC intensity. The low R^2 value (0.24) demonstrated the lack of conclusive relationship between the middle eyewall slope and TC intensity (Table 2). The smaller magnitude of the middle eyewall slope as compared to the lower and mid-lower eyewall slopes physically indicated a less upright upper eyewall. Despite the lack of relationship between slope and intensity in the upper and middle eyewall, the

consistent relationship between slope and intensity in the lower eyewall indicates that with continued research, slope calculations may one day be used to estimate current TC intensity, which would be a new operational technique.

4. Conclusions and Future Research

In this study, the average IR brightness temperatures were computed at four points in the TC inner core: the start of the lower, middle, and upper eyewalls, and the limit of the upper eyewall. Eyewall slopes were also computed in the lower, mid-lower, upper-lower, and middle eyewalls. The IR Tb averages at the start and limit of the upper eyewall were found to be negatively related to TC intensity. Physically, this signifies that taller clouds (measured by brightness temperature) were linked to the primary circulation (measured by TC intensity). Additionally, eyewall slope in the lower and mid-lower eyewalls showed a consistent negative relationship with TC intensity. Physically, this suggests that the lower regions of the eyewall were more upright in more intense TCs.

Brightness temperature averages at the start of the lower and middle eyewalls showed no conclusive relationship to TC intensity. However, a potentially interesting phenomenon was observed at the start of the lower eyewall once TC intensity exceeded 100 knots. While the highest value of IR Tb averages at the start of the lower eyewall remained roughly constant for all intensities, the lowest value increased with greater TC intensity after 100 knots, warming from 195K at 100 knots to 240K at 150 knots. This observation may be linked to studies of TC eye thermodynamics, which conclude that warming in the eye occurs concurrently with intensification (Stern and Zhang 2012). While the start of the lower eyewall is not located in the eye itself, it denotes the transition from the warm brightness temperatures of the cloud-free eye to the cold brightness temperatures of the eyewall cloud tops. As such, observations of the lower eyewall may reflect some of the processes occurring in the TC eye. Further investigation is required to determine if the location of the minimum IR Laplacian shares thermodynamic characteristics with the eye, eyewall, or both.

Further investigation is warranted to assess whether the eyewall points determined in this study would demonstrate a consistent relationship to wind fields, thus yielding another connection between structure and intensity. Kossin et al. (2007) related eye radius in IR data, calculated using mean cloud-top brightness temperatures, to the radius of maximum wind. The RMW, the location of the maximum primary circulation, is usually located within a few kilometers inward of the maximum secondary circulation (Kossin et al. 2007). The eyewall points defined in this study could be identified in TCs with accompanying aircraft reconnaissance data, and related to the RMW, or the radii of 34, 50, and 64 knot winds.

The slope component of this study corroborated Hazelton and Hart's (2013) findings that more upright eyewalls correspond to greater TC intensity. Furthermore, this study identified a consistent negative relationship between eyewall slope and increased intensity using geostationary satellite data, which is an operational product available between every 30 minutes to several hours, much more frequently than aircraft data, and is relied upon by forecasters in ocean basins who do not have the luxury of aircraft reconnaissance programs for *in-situ* measurements. Due to the moderate correlation of the lower and mid-lower eyewall slopes to TC intensity demonstrated in this study, it would be valuable to apply the IR and WV-IR data analysis methods used here to geostationary satellite data in real time, aiding in objective assessment of current intensity and structure of TCs.

APPENDIX

The five tropical cyclones analyzed in this study varied greatly in intensity, duration, and structural characteristics. Two of the TCs, Super Typhoons Sanba and Jelawat, typified the extremely intense, symmetrical TC type; on the other hand, Typhoon Prapiroon was on the weaker spectrum of typhoons, reaching a maximum intensity just above 100 knots, and fluctuated between a closed and open, ragged eyewall. Most of the TCs in this study experienced a period of rapid structural and/or intensity change during the period of analysis. Three TCs (Sanba, Bolaven, and Son-Tinh) underwent episodes of explosive intensification during their lifetime, and all the examined TCs but Typhoon Prapiroon developed concentric eyewalls. Understanding the important events in the lifecycles of these typhoons aids in linking intensity and structural processes to the IR Tb averages and eyewall slopes calculated in this study.

Presented in this appendix are synoptic summaries of the five typhoons analyzed in this study. Both the geostationary satellite data examined in this study and microwave imagery from the Marine Meteorology Division at the Naval Research Laboratory, Monterey were used in preparing the lifecycle analysis presented here. Tropical cyclone intensities were obtained from the Joint Typhoon Warning Center's warning products. Finally, discussions of the environmental factors impacting each TC were obtained from the Joint Typhoon Warning Center's Prognostic Reasoning discussions, which explain the current and forecasted situation over the lifetime of a TC.

I. Super Typhoon Sanba Synoptic Summary

Typhoon Sanba exhibited visually identifiable eyes for roughly 4 days. The period of analysis lasted from 1901 UTC 12 September 2012 to 1714 UTC 16 September 2012. The TC spent approximately 4.75 days above typhoon intensity; all but approximately twelve hours of the duration of typhoon intensity are encompassed during the period of study. For the majority of its lifetime, Typhoon Sanba was mostly symmetric, featuring a circular, well-defined eye and broad, intense eyewall. An episode of rapid intensification and eyewall replacement cycle caused the most significant structural and intensity changes in Typhoon Sanba during the period of study.

Typhoon 17W (Sanba) reached tropical storm strength at 0600 UTC 11 September 2012, at 11.1° N and 133.8° E, east of the Philippines (Fig. A1a) (JTWC 2012). Sanba reached typhoon intensity 24 hours later (Fig. A1b) under conditions of low wind shear (<10 knots) and strong outflow (JTWC 2012). A central dense overcast (CDO) obscured the identification of structural features for twelve hours, until the TC organized to a point where the eye was visible in IR imagery, near 1900 UTC 12 September 2012, beginning the period of this study (Fig. A2a). Five hours after the eye became visible, steered by the subtropical ridge to the east, Typhoon Sanba assumed a predominately-northward track with little longitudinal movement (Fig. A1a) (JTWC 2012).

Typhoon Sanba underwent an episode of rapid intensification between 0000-1200 UTC 13 September 2012, when maximum tangential wind velocities increased 50 knots in 12 hours, from 90 knots to 140 knots (Fig. A1b) (JTWC 2012). At 1800 UTC, the TC achieved its overall maximum tangential windspeed, an estimated 150 knots (JTWC 2012). At maximum intensity, Super Typhoon Sanba displayed a broad eyewall and spiral rainband structure (Fig. A2b). Super

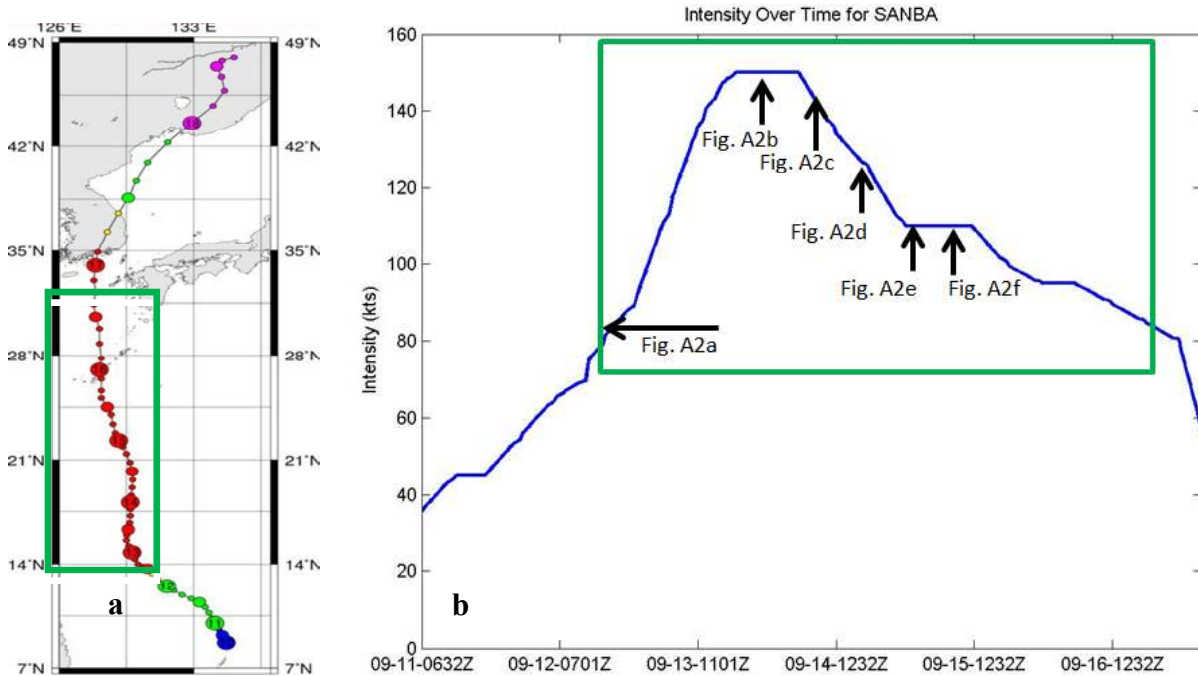


Figure A1: Intensity over Super Typhoon Sanba's lifecycle. Green boxes outline portion of the lifecycle analyzed in this study. (a) Storm track with colored circles indicate intensity by category: blue denotes a tropical disturbance; green, a tropical depression; yellow, a tropical storm; red, a typhoon; and purple, an extratropical cyclone (after <http://agora.ex.nii.ac.jp/digital-typhoon/summary/wnp/1/201216.html.en>). (b) Maximum tangential wind speed (kts) over time (UTC). Arrows and figure numbers denote the times and intensities of the satellite imagery in Fig. A2a-f.

Typhoon Sanba's intensity then began to decline after 1200 UTC 14 September 2012, and the TC's eye and eyewall structure became compact as its intensity dropped to 135 knots (JTWC 2012) (Fig. A2d).

An eyewall replacement cycle began early on 14 September, heralding a period of structural changes and intensity fluctuations; microwave imagery indicated concentric eyewalls at 0542 UTC 14 September 2012 (Fig. A2c). Microwave imagery from 16.5 hours later showed that the primary eyewall had weakened significantly (Fig. A2e). The primary eyewall, which had decayed into a small semicircle, protruded into the widened TC eye, and was surrounded by the strengthened secondary eyewall (Fig. A2e). By 0630 UTC 15 September 2012, the primary eyewall had dissipated, leaving behind a large eye, which then expanded further (Fig. A3f).

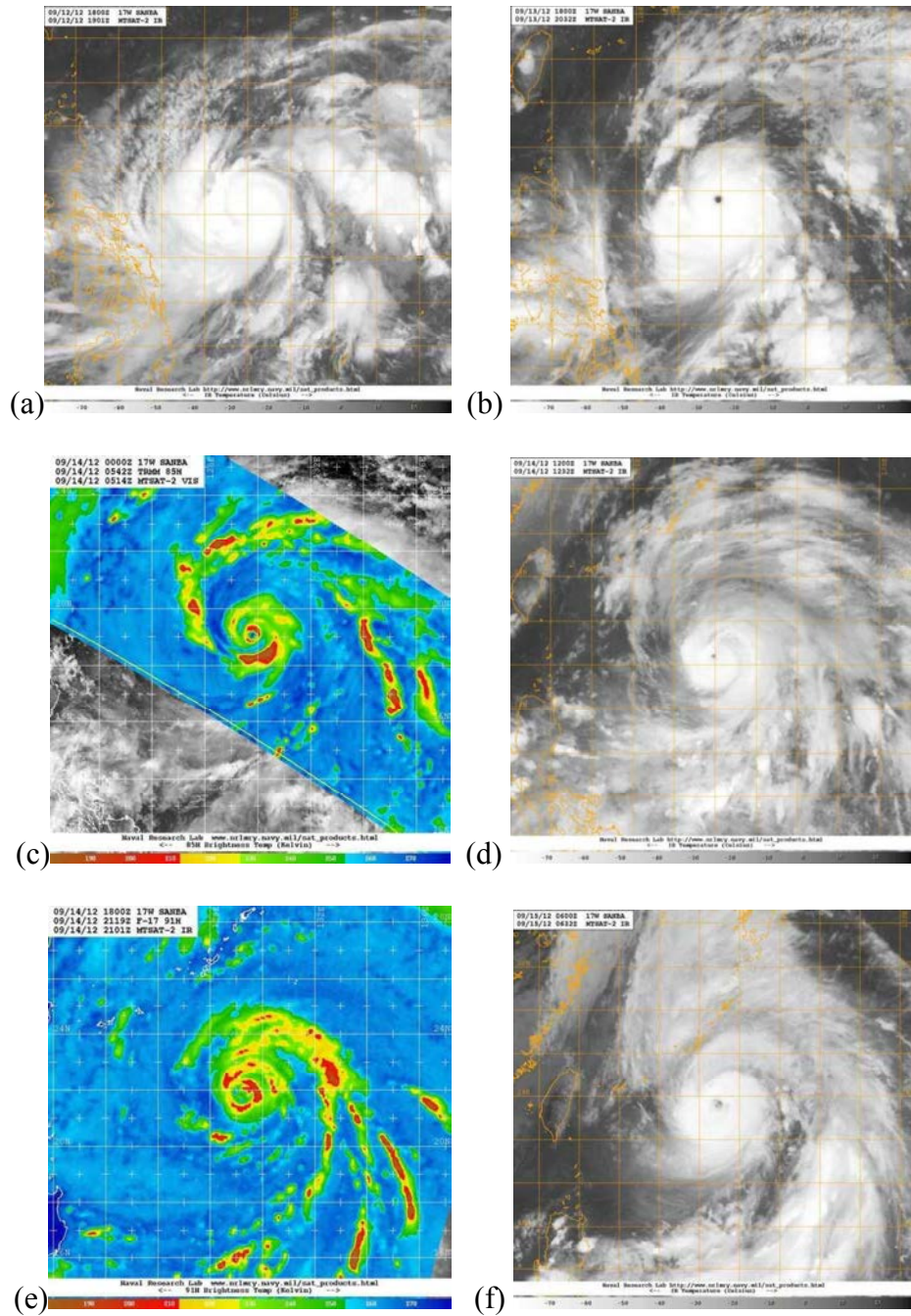


Figure A2. Geostationary infrared (a,b,d,f) and microwave (c,e) imagery of Typhoon Sanba at: (a) 1900 UTC 12 September 2012, (b) 2032 UTC 13 September 2012, (c) 0542 UTC 14 September 2012, (d) 1232 UTC 14 September 2012, (e) 2119 UTC 14 September 2012, (f) 0430 UTC 15 September 2012. The IR images are from the MTSAT-2 and the microwave images are from the (c) TRMM (Tropical Rainfall Measuring Mission) and (e) F-17 satellites. Imagery courtesy NRL Monterey (http://www.nrlmry.navy.mil/tc-bin/tc_home2.cgi).

While these stages of eyewall replacement occurred, Typhoon Sanba's intensity, which had been dropping steadily, plateaued at 110 knots (Fig. A1b) (JTWC 2012).

After 1200 UTC 15 September 2012, the intensity in Typhoon Sanba began to diminish again (Fig. A1b) (JTWC 2012). Seven hours later, the wide eye began to contract, completing the eyewall replacement cycle as it returned to the original eye radius. The contraction of the eye coincided roughly with Typhoon Sanba's passage over the island of Okinawa, which, along with greater vertical wind shear (10-20 knots) and colder sea surface temperatures, further weakened the TC to 95 knots (JTWC 2012). Typhoon Sanba's outer rainbands began to affect the Japanese island of Kyushu around 1500 UTC 16 September 2012 (Fig. A1a) (JTWC 2012). Typhoon Sanba quickly became disorganized; the eye was no longer visually identifiable after 1714 UTC 16 September 2012, which coincided with the termination of analysis for this TC. It made official landfall on the Korean Peninsula on 0100 UTC 17 September 2012, and later completed extratropical transition (Fig. A1a) (JTWC 2012).

II. Typhoon Bolaven Synoptic Summary

Typhoon Bolaven featured visually identifiable eyes for roughly 2.5 days. The period of analysis spanned from 0232 UTC 24 August 2012 to 1832 UTC 26 August 2012. Typhoon Bolaven remained above 100 knots and featured narrow eyewalls and rainbands for the entirety of the period of study. Structural features were obscured by CDO for the remainder of the TC's lifecycle, which included the majority of the typhoon's intensification. By the time the TC eye became visible, Typhoon Bolaven had already reached 105 knots (JTWC 2012). Structural and intensity fluctuations during the period of analysis were dominated by an eyewall replacement cycle.

Typhoon Bolaven reached tropical storm strength at 0600 UTC 20 August 2012, at 17.6° N and 141.7° E, west of the Marianas islands, and reached typhoon intensity 30 hours later, at 1200 UTC 21 August 2012 (Fig. A3a) (JTWC 2012). Because the eye of the TC was obscured by CDO, analysis for the purpose of this research did not begin until the cover dissipated at 0232 UTC 24 August 2012. At this time, Typhoon Bolaven exhibited a small eye, surrounded by several tiers of wrapping rainbands (Fig. A4a). Wind shear values decreased during the same timeframe and Typhoon Bolaven continued to intensify (JTWC 2012). Typhoon Bolaven reached its maximum tangential wind speed of 125 knots at approximately 1800 UTC 24 August 2012 (Fig. A3b) (JTWC 2012). Almost immediately after achieving maximum intensity, at 2000 UTC 24 August 2012, Typhoon Bolaven began an eyewall replacement cycle, beginning a period of structural change and fluctuating intensity that would continue for the remainder of the analysis period.

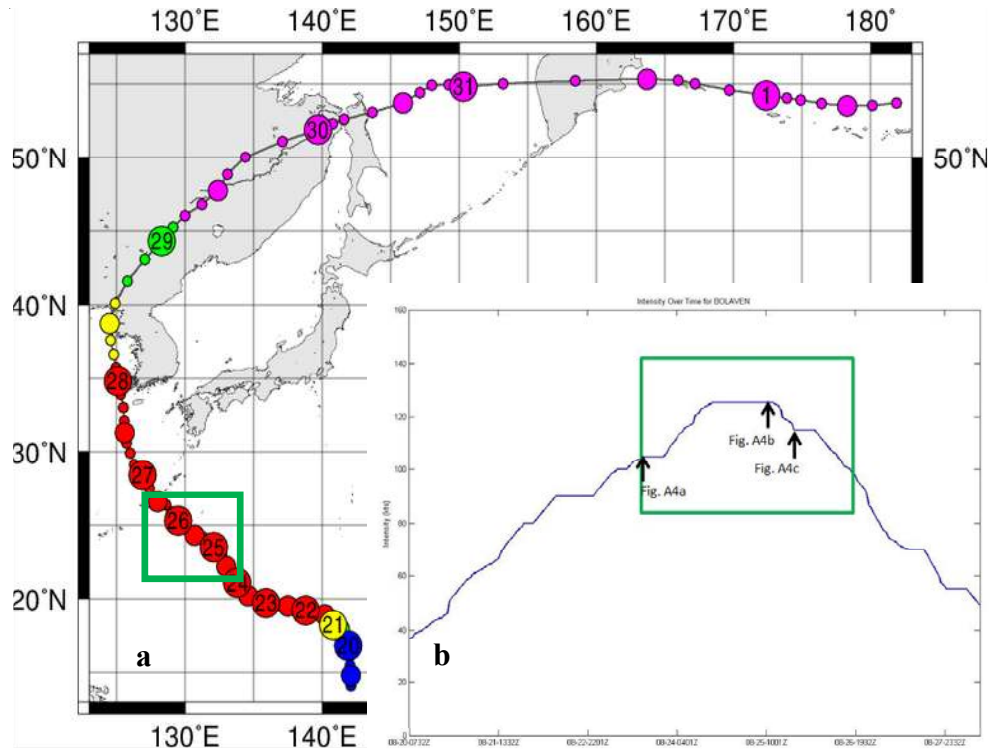


Figure A3: As in Figure A1, except for Typhoon Bolaven (after <http://agora.ex.nii.ac.jp/digital-typhoon/summary/wnp/1/201215.html.en>).

At the beginning of the eyewall replacement cycle, a concentric eyewall, approximately 0.5° latitude from the eye, surrounded the primary eyewall and was visible in the microwave imagery (Fig. A4b). As time progressed on 25 August, the primary eyewall weakened, and the banding of the primary and secondary eyewalls, as well as the peripheral rainbands, became clearer in the IR imagery (Fig. A4c). The primary eyewall began to dissipate 34 hours after the eyewall replacement cycle started, which led to a slight, brief widening of the eye area at 0600 UTC 26 August 2012. For 6 hours, between 1200-1800 UTC 26 August 2012, Typhoon Bolaven's rainbands passed over Okinawa and other islands in the archipelago (Fig. A3a) (JTWC 2012). The almost-completed eyewall replacement, interaction with land, and passage into colder sea surface temperatures all contributed to a weakening of Typhoon Bolaven to 100 knots (JTWC 2012). As Typhoon Bolaven weakened, it became disorganized; the eye was no longer visible at 1800 UTC 26 August 2012, concluding the duration of study.

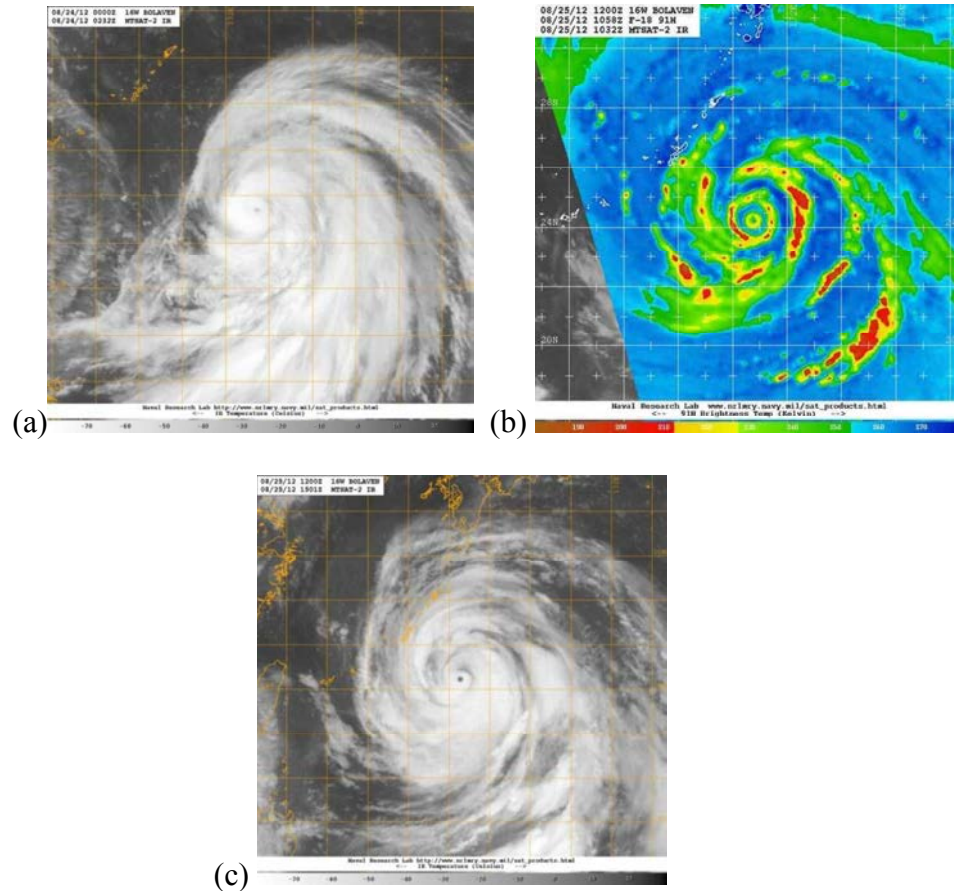


Figure A4. Geostationary infrared (a,c) and microwave (b) imagery of Typhoon Bolaven at (a) 0230 UTC 24 August 2012, (b) 1058 UTC 25 August 2012, and (c) 1500 UTC 25 August 2012. The IR images are from the MTSAT-2 and the microwave image is from the F-18 satellite. Imagery courtesy NRL Monterey (http://www.nrlmry.navy.mil/tc-bin/tc_home2.cgi).

Throughout 27 August, Typhoon Bolaven weakened significantly due to colder sea surface temperatures and increased wind shear. The TC was downgraded to tropical storm classification at 0000 UTC 28 August 2012 (JTWC 2012). Tropical Storm Bolaven made landfall at the North Korean/Chinese border around 1200 UTC 28 August 2012 and weakened further into a tropical depression before undergoing extratropical transition (Fig. A3a) (JTWC 2012).

III. Super Typhoon Jelawat Synoptic Summary

Typhoon Jelawat featured visually identifiable eyes for approximately 6.5 days. The period of study lasted from 2232 UTC 22 September 2012 to 0632 UTC 29 September 2012. Typhoon Jelawat sustained winds at or above typhoon intensity for 7.25 days, the longest period of the five storms analyzed in this study. Typhoon Jelawat featured a well-defined eye and broad, deeply convective eyewall for most of its lifecycle. An episode of rapid intensification, an eyewall replacement cycle, and the later formation of another secondary eyewall were the chief influences on intensity and structure during the analysis period.

Typhoon Jelawat reached tropical storm strength at 0600 UTC 20 September 2012, at 13.2° N and 131.7° E, east of Guam (Fig. A5a) (JTWC 2012). Two days later, Tropical Storm Jelawat developed a central, dense overcast that persisted for 16.5 hours, obscuring most structural features in the IR and WV imagery. Tropical Storm Jelawat intensified in the warm waters of the Philippine Sea in an area of low wind shear, reaching typhoon intensity at 1800 UTC 22 September 2012 (Fig. A5b) (JTWC 2012). The burgeoning Typhoon Jelawat developed an identifiable pinhole eye 4.5 hours after reaching typhoon intensity, at 2232 UTC 22 September 2012, marking the start of the analysis period.

At 0000 UTC 23 September 2012, Typhoon Jelawat began an episode of rapid intensification, with tangential wind velocities increasing 65 knots in 18 hours, from 65 to 130 knots (Fig. A5b) (JTWC 2012). During the episode of rapid intensification, several broad rainbands with very cold cloud tops propagated away from the center of the TC (Fig. A6a). After Typhoon Jelawat reached 130 knots at 1200 UTC 23 September 2012, it remained at that intensity for 24 hours, during which time IR and WV imagery showed a well-organized TC with several rainbands spiraling around the eyewall (JTWC 2012).

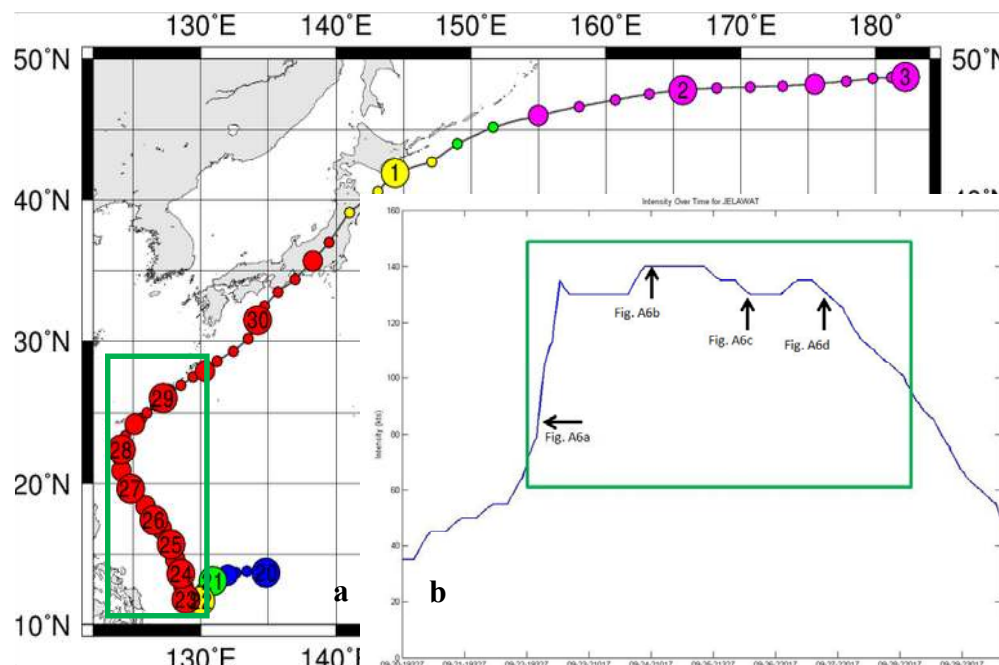


Figure A5: As in Figure A1, except for Super Typhoon Jelawat. (after <http://agora.ex.nii.ac.jp/digital-typhoon/summary/wnp/1/201217.html.en>)

The eye and eyewall widened around 0900 UTC 24 September 2012 after the outer bands of Super Typhoon Jelawat brushed the Philippine Islands (JTWC 2012). Two days after reaching typhoon intensity, Super Typhoon Jelawat reached maximum intensity of 140 knots at 1800 UTC 24 September 2012, with a broad band of intense convection marking the eyewall (JTWC 2012).

Around 0000 UTC 25 September 2012, Super Typhoon Jelawat began an eyewall replacement cycle, starting a time of structural and intensity variation. Two eyewalls are visible in the microwave imagery; the concentric eyewall is located approximately 1° in latitude from the TC eye (Fig. A6b). Later on 25 September, the primary eyewall weakened. Super Typhoon Jelawat began to decline in intensity between 1800 UTC 25 September 2012 and 0000 UTC 26 September 2012, from 140 knots to 135 knots (JTWC 2012). At 0930 UTC 26 September 2012, a weak primary eyewall persisted, separated from the secondary eyewall by a moat.

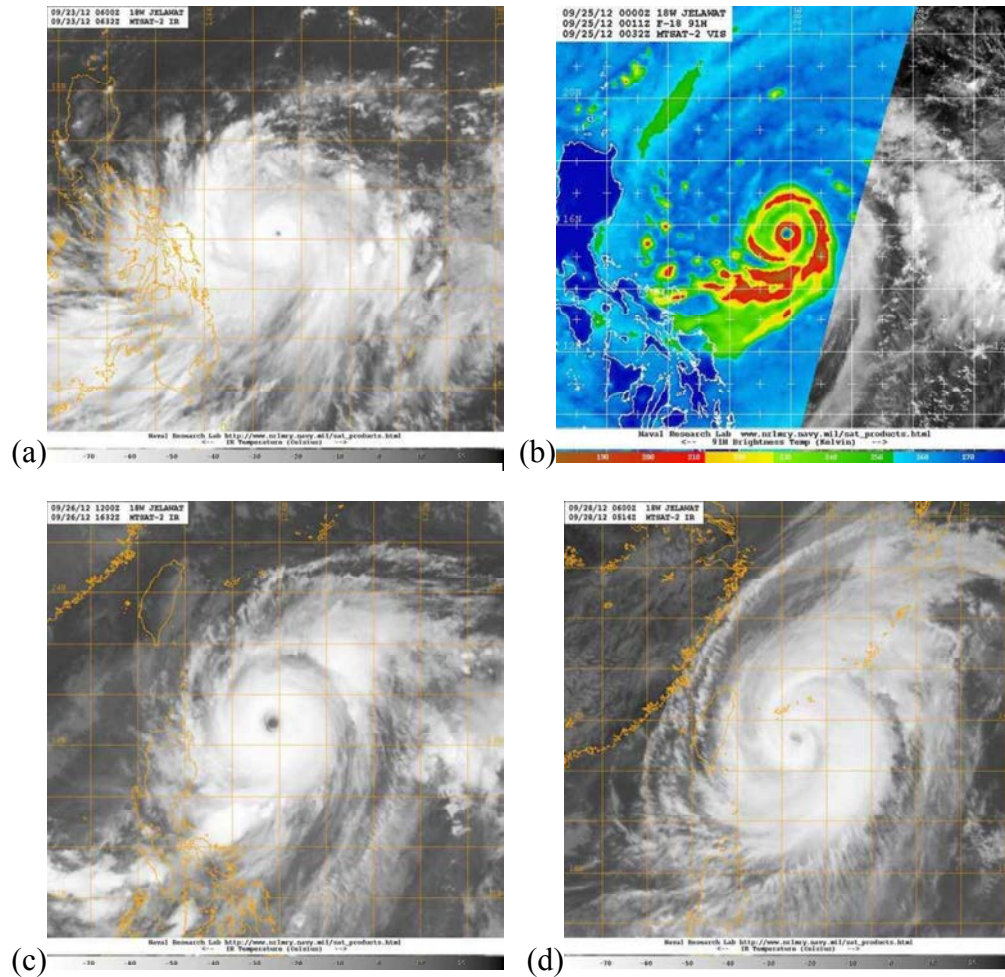


Figure A6. Geostationary infrared (a,c,d) and microwave (b) imagery of Typhoon Jelawat at (a) 0632 UTC 23 September 2012, (b) 0011 UTC 25 September 2012, (c) 1632 UTC 26 September 2012, and (d) 0514 UTC 28 September 2012. The IR images are from the MTSAT-2 and the microwave image is from the F-18 satellite. Imagery courtesy NRL Monterey (http://www.nrlmry.navy.mil/tc-bin/tc_home2.cgi).

After 1200 UTC 26 September 2012, Super Typhoon Jelawat's intensity plateaued at 130 knots (JTWC 2012). At 1632 UTC 26 September 2012, the weak primary eyewall dissipated completely, leading to a further widening of the eye (Fig. A6c).

Between 0000-0600 UTC 27 September 2012, Super Typhoon Jelawat's intensity resurged briefly to 135 knots (JTWC 2012). For the next twelve hours, the TC displayed a wide eye and broad, deeply convective eyewall. Between 1800 UTC 27 September 2012 and 0000 UTC 28 September 2012, the eye shrank and cloud tops in Super Typhoon Jelawat began to

warm. Concurrent with the warming trend, intensity dropped to 125 knots by 0000 UTC 28 September 2012 (JTWC 2012).

Between 0000-0600 UTC 28 September 2012, Typhoon Jelawat developed a more spiral, asymmetric structure, and a narrower eye than before. Microwave imagery indicated concentric eyewalls, and intensity continued to decrease. Later on 28 September, Typhoon Jelawat brushed by Taiwan, and the spiral rainband in its northeast quadrant elongated (Fig. A6d) (JTWC 2012). Between 1200-1630 UTC 28 September 2012, dry air was entrained into the TC between the concentric eyewalls and spiral rainbands (Fig. A9d). During that timeframe and beyond, intensity continued to decrease (Fig. A5b).

After 0630 UTC 29 September 2012, the eye was almost entirely clouded over, ending the period of analysis for this storm. Typhoon Jelawat became increasingly disorganized as it tracked towards Japan, making landfall on the Japanese island of Honshu around 0900 UTC 30 September 2012 as a tropical storm (JTWC 2012). Tropical Storm Jelawat continued into the Sea of Japan, where it completed extratropical transition (JTWC 2012).

IV. Typhoon Prapiroon Synoptic Summary

Typhoon Prapiroon featured visually identifiable eyes for 5 days. There were two separate periods of analysis: from 1901 UTC 10 October 2012 to 1032 UTC 13 October 2012, and again from 1632 UTC 13 October 2012 to 0232 UTC 16 October 2012. The eyewall dissipated completely between the two periods of visible eyes, rendering analysis impossible in the interim. Typhoon Prapiroon's maximum intensity (100 knots) was less than any other storm examined in this study (JTWC 2012). Structural and intensity characteristics over Typhoon Prapiroon's lifetime were dominated by its poor organization; much of the time, Prapiroon lacked a complete eyewall and showed a large, ragged eye.

Typhoon Prapiroon began as a disorganized region of convection northeast of Guam, and moved northwestward for several days before reaching tropical storm strength at 1800 UTC 07 October 2012 (Fig. A7a) (JTWC 2012). Over the next 30 hours, convective bursts expanded significantly in the area to the south and west, and Prapiroon reached typhoon status at 0000 UTC 09 October 2012 (Fig. A7b) (JTWC 2012).

At 1900 UTC 10 October 2012, while Typhoon Prapiroon maintained an intensity of 90 knots, an eye became and remained visible, beginning the period of analysis for this study (JTWC 2012) (Fig. A8a). Between 0130-0930 UTC 11 October 2012, a band of dry air was entrained into the TC, interfering with the formation of a well-defined eye and intensification. The eye was ragged and asymmetric until 0930 UTC 11 October 2012, when multiple regions of warmer brightness temperatures in the center of the TC coalesced into a single, circular eye. Typhoon Prapiroon reached its maximum velocity of 100 knots at 1800 UTC 11 October 2012.

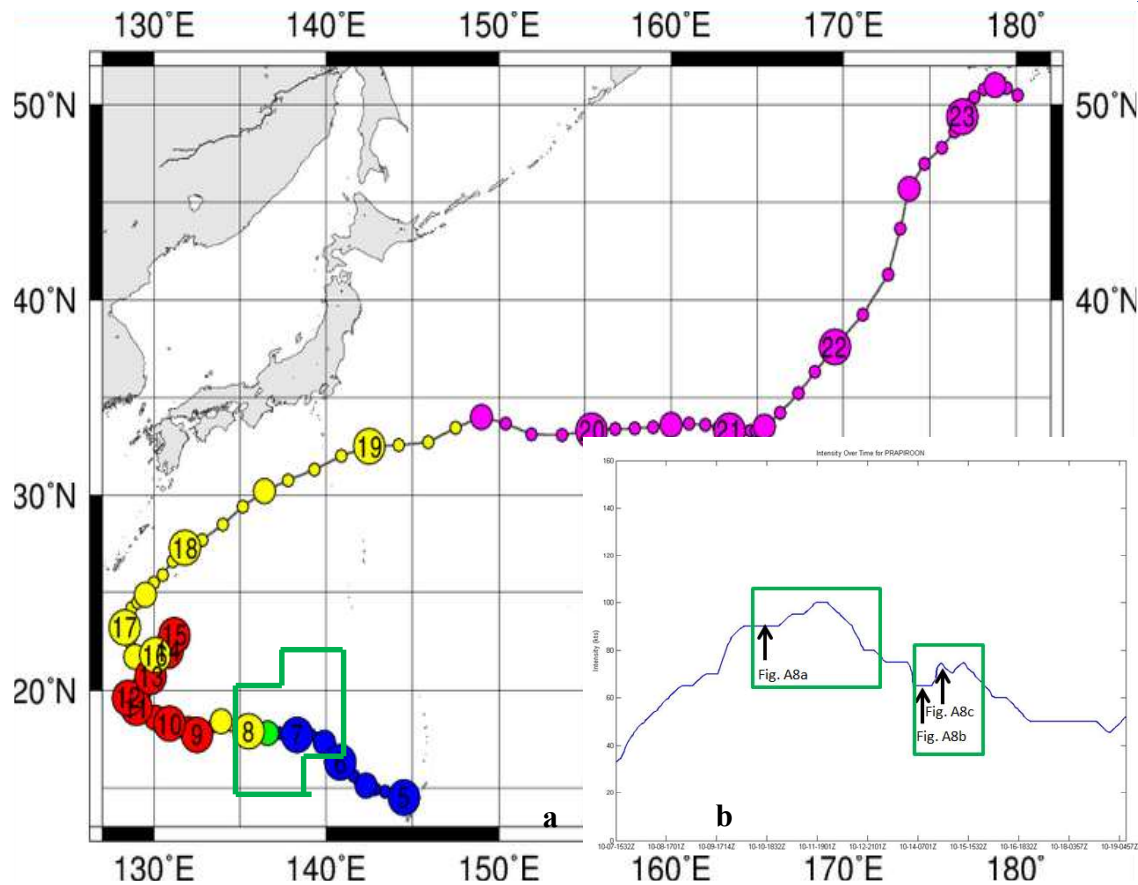


Figure A7: As in Figure A1, except for Typhoon Prapiroon. (after <http://agora.ex.nii.ac.jp/digital-typhoon/summary/wnp/l/201221.html.en>)

Between 0000-0600 UTC 12 October 2012, Typhoon Prapiroon began to decline in intensity, and cloud top brightness temperatures warmed noticeably in the IR imagery (JTWC 2012). In the same timeframe, a band of dry air was entrained into the TC between the rainbands and eyewall. During the next six hours, cold convective cloud tops to the north of the eye dissipated. After 0330 UTC 13 October 2012, Typhoon Prapiroon had re-organized; IR imagery showed a whole but weak eyewall and spiral rainband structure, and TC intensity plateaued at 75 knots.

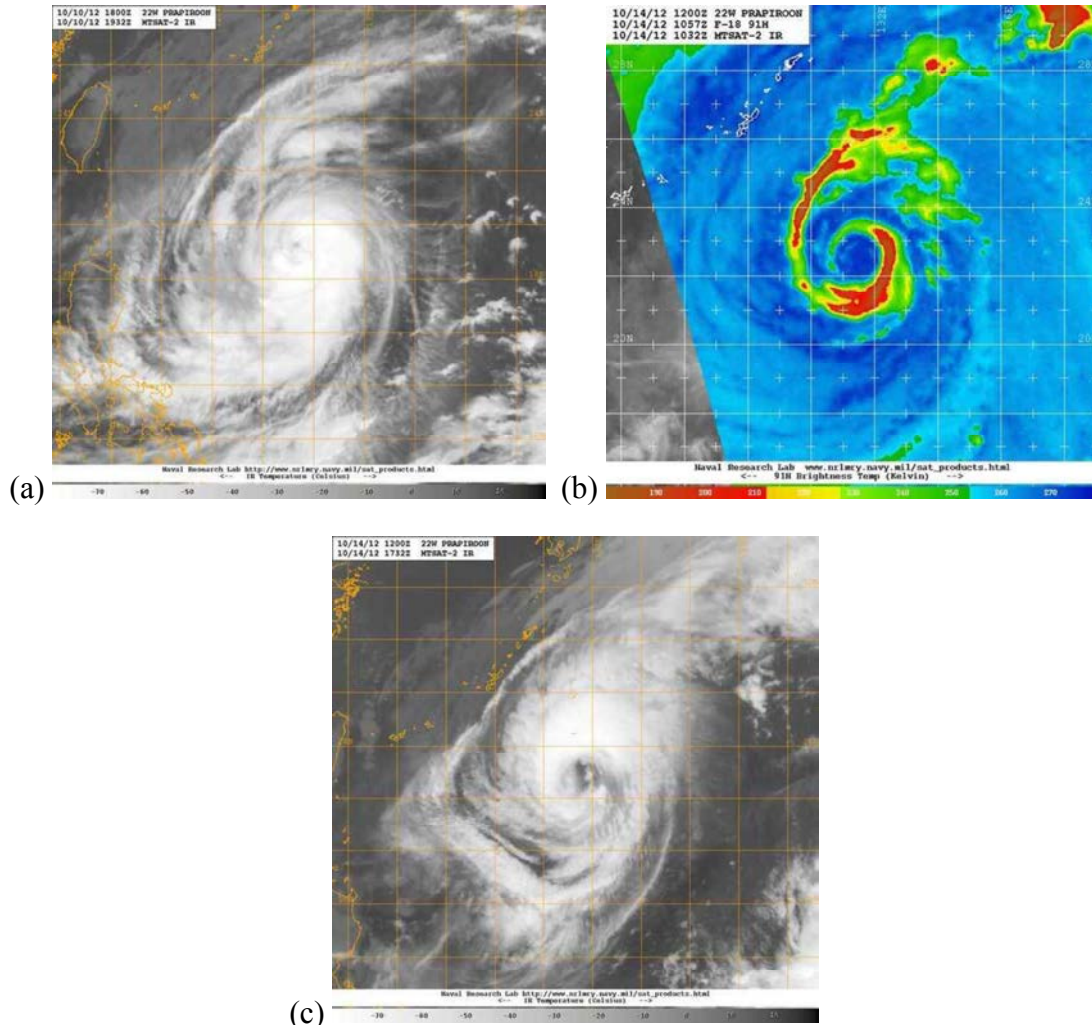


Figure A8: Geostationary infrared (a,c) and microwave (b) imagery of Typhoon Prapiroon at (a) 1932 UTC 10 October 2012, (b) 1057 UTC 14 October 2012, and (c) 1732 UTC 14 October 2012. The IR images are from the MTSAT-2 and the microwave image is from the F-18 satellite. Imagery courtesy NRL Monterey (http://www.nrlmry.navy.mil/tc-bin/tc_home2.cgi).

Cloud top brightness temperatures in the eyewall increased, indicating weakening, between 1630 UTC 13 October 2012 and 0300 UTC 14 October 2012, when the eyewall began to disintegrate (Fig. A8b), and TC intensity decreased to 65 knots concurrently (JTWC 2012). Between 1730 UTC 14 October 2012 and 0000 UTC 15 October 2012, a rainband with cold cloud tops wrapped completely around the large eye, and Typhoon Prapiroon's intensity resurged to 75 knots (JTWC 2012) (Fig. A8c).

At 0300 UTC 15 October 2012, convection in the northern half of the TC began to dissipate, and cloud tops in the entire system warmed. Nine hours later, Typhoon Prapiroon's intensity began to decrease once again (JTWC 2012). The TC was somewhat re-organized by 1700 UTC 15 October 2012, though cloud top brightness temperatures were still quite warm and the eyewall was not closed.

After 0000 UTC 16 October 2012, Prapiroon downgraded to tropical storm classification, and its organization disintegrated quickly (JTWC 2012). A TC eye was no longer distinguishable 2.5 hours later, at 0232 UTC 16 October 2012, ending the period of analysis. Tropical Storm Prapiroon became further disorganized accelerated quickly to the northeast, and completed extratropical transition around 1200 UTC 19 October 2012 (JTWC 2012).

V. Typhoon Son-Tinh Synoptic Summary

Typhoon Son-Tinh possessed a visually identifiable eye for less than one day. The period of examination spanned from 0257 UTC 27 October 2012 to 2330 UTC 27 October 2012. It sustained typhoon-strength winds for only approximately 2 days. Rapid intensification occurred during the brief period of visible eyes, dominating structural and intensity changes; a secondary eyewall formed as well, also affecting structure and intensity.

Typhoon Son-Tinh reached tropical storm strength at 0000 UTC 24 October 2012, located around 520 miles southeast of Manila, near the Philippine island of Mindanao (Fig. A9a) (JTWC 2012). For several days, then-Tropical Storm Son-Tinh tracked over the Visayas island chain of the Philippines, preventing its intensification or organization.

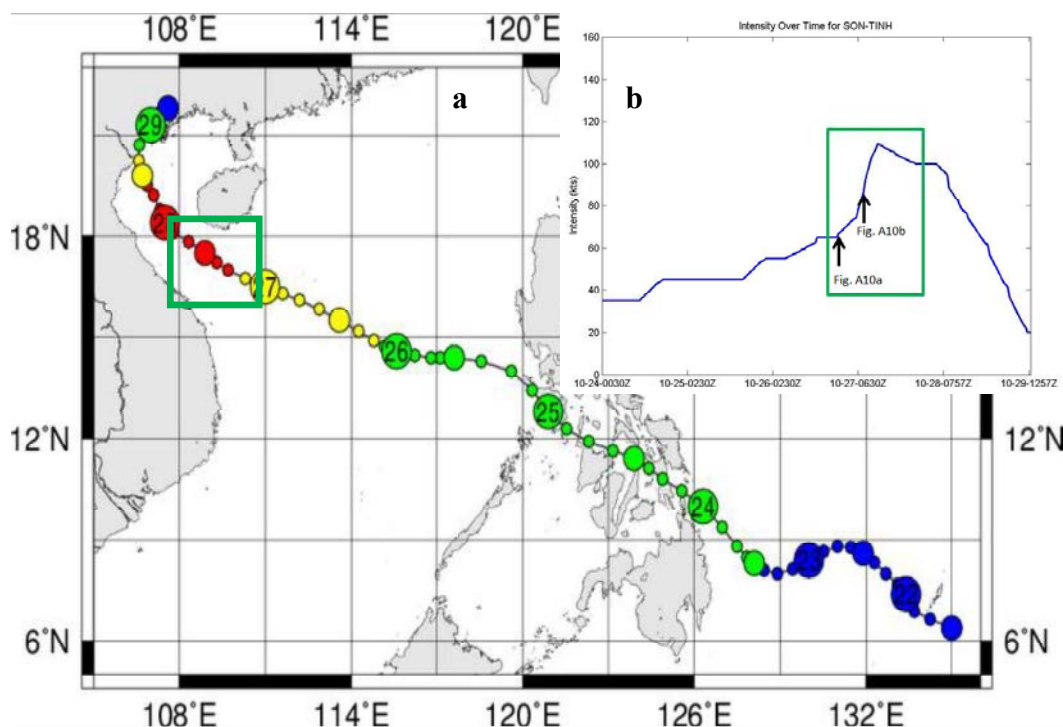


Figure A9: As in Figure A1, except for Typhoon Son-Tinh. (after <http://agora.ex.nii.ac.jp/digital-typhoon/summary/wnp/1/201223.html.en>)

As 26 October progressed, Son-Tinh became better organized, and reached typhoon status at 1800 UTC 26 September 2012, commencing the period of study (Fig. A9b) (JTWC

2012). An eye became visible in the IR and WV imagery at 0257 UTC 27 October 2012 (Fig. A10a). Between 0000-1200 UTC 27 October 2012, Typhoon Son-Tinh rapidly intensified, gaining 45 knots in 12 hours; TC intensity increased from 65 to 110 knots, the TC's maximum tangential windspeed (Fig. A9b) (JTWC 2012). Infrared brightness temperature averages in the upper eyewall were the coldest observed in Typhoon Son-Tinh while the TC underwent rapid intensification and reached its maximum wind speed (Figs. 9a,b).

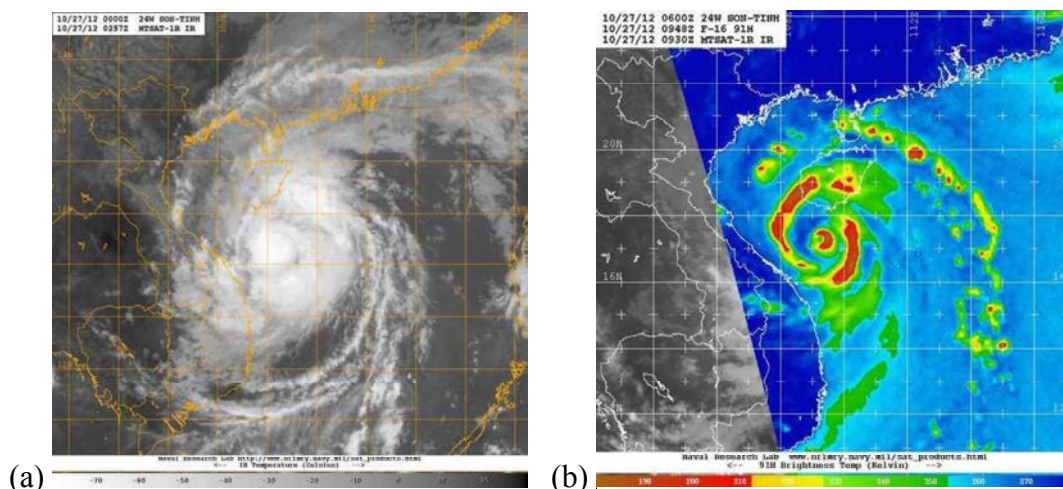


Figure A10: Geostationary infrared (a) and microwave imagery (b) of Typhoon Son-Tinh at: 0257 UTC 27 October 2012, and (b) 0948 UTC 27 October 2012. The IR images are from the MTSAT-2 and the microwave image is from the F-16 satellite. Imagery courtesy NRL Monterey (http://www.nrlmry.navy.mil/tc-bin/tc_home2.cgi).

Concentric eyewalls were visible in microwave imagery at 0948 UTC 27 October 2012 (Fig. A10b). At 1800 UTC 27 October 2012, while concentric eyewalls were visible, intensity began to decrease (Fig. A9b) (JTWC 2012). The typhoon eye clouded over at 2330 UTC 27 October 2012, after being visible for less than one day, ending the brief period of study. The TC was downgraded to a tropical storm 30 hours later, and recurved to the east during the latter part of 29 October before making landfall in southern China (Fig. A9a) (JTWC 2012).

REFERENCES

- Committee for Earth Observation Studies, cited 2012: CEOS EO HANDBOOK- INSTRUMENT SUMMARY-IMAGER/MTSAT-2. [Available online at <http://database.eohandbook.com/database/instrumentsummary.aspx?instrumentID=466>]
- Didlake, A. C. and R. A. Houze, Jr., 2012: Convective-scale variations in the inner-core rainbands of a tropical cyclone. *J. Atmos. Sci.*, **70**, 504-523.
- Dunion, J., C. Thorncroft, C. S. Velden, K. Emanuel, and D. S. Nolan, 2012: Diurnal pulsing of tropical cyclones: an overlooked yet fundamental TC process? *Proc. 30th Conference on Hurricanes and Tropical Meteorology*, Ponte Vedra Beach, FL.
- Dvorak, V. F., 1975: Tropical cyclone intensity analysis and forecasting from satellite imagery. *Mon. Wea. Rev.*, **103**, 420-430.
- , 1984: Tropical cyclone intensity analysis using satellite data. NOAA Tech. Rep. 11, 45 pp.
- Frank, W. M., 1977: The structure and energetics of the tropical cyclone I. Storm structure. *Mon. Wea. Rev.*, **105**, 1119-1135.
- Fritz, S., and I. Laszlo, 1993: Detection of water vapor in the stratosphere over very high clouds in the tropics. *J. Geophys. Res.*, **98** (D12), 22,959-22,967.
- Gray, W. M., 1968: Global view of the origin of tropical disturbances and storms. *Mon. Wea. Rev.*, **96**, 669-700.
- Hazleton, A. T. and R. E. Hart, 2013: Hurricane eyewall slope as determined from airborne radar reflectivity data: composites and case studies. *Wea. Forecasting*, **28**, 368-386.
- Herndon, D. and C. S. Velden, 2007: CIMSS TC Intensity Satellite Consensus (SATCON). *Proc. 61st Interdepartmental Hurricane Conference*, New Orleans, LA.
- Houze Jr., R. A., 2010: Clouds in tropical cyclones. *Mon. Wea. Rev.*, **138**, 293-344.
- , S. S. Chen, B. F. Smull, W. C. Lee, and M. M. Bell, 2007: Hurricane intensity and eyewall replacement. *Science*, **315**, 1235-1239.
- Japan Meteorological Agency, cited 2012: Basic information on MTSAT-1R and 2. [Available online at http://www.jma.go.jp/jma/jma-eng/satellite/mtsats1r/Basic_information_on_MTSAT-1R_and_2.html]
- Joint Typhoon Warning Center, 2012: Prognostic Reasoning for Super Typhoon 16W. 1800 UTC 24 September 2012 – 0600 UTC 27 September 2012. [Available online at

- <http://www.woeurope.eu/cgi-app/tropicstorm?LANG=eu&GEBIET=sep&STURM=wp17&ADV=discus&ZEIT=201209132100>]
- , 2012: Prognostic Reasoning for Super Typhoon 18W. 1800 UTC 24 September 2012 – 0600 UTC 27 September 2012. [Available online at <http://www.woeurope.eu/cgi-app/tropicstorm?LANG=eu&GEBIET=sep&STURM=wp18&ADV=discus&ZEIT=201209242100>]
- , 2012: Prognostic Reasoning for Tropical Storm 16W. 0600 UTC 20 August 2012 – 1200 UTC 21 August 2012, 0000-1200 UTC 28 August 2012. [Available online at <http://www.woeurope.eu/cgi-app/tropicstorm?LANG=eu&GEBIET=sep&STURM=wp16&ADV=discus&ZEIT=201208200900>]
- , 2012: Prognostic Reasoning for Tropical Storm 17W. 0600 UTC 11 September 2012. [Available online at <http://www.woeurope.eu/cgi-app/tropicstorm?LANG=eu&GEBIET=sep&STURM=wp17&ADV=discus&ZEIT=201209110900>]
- , 2012: Prognostic Reasoning for Tropical Storm 18W. 1800 UTC 20 September 2012 – 1200 UTC 22 September 2012, 1 pp. [Available online at <http://www.woeurope.eu/cgi-app/tropicstorm?LANG=eu&GEBIET=sep&STURM=wp18&ADV=discus&ZEIT=201209202100>]
- , 2012: Prognostic Reasoning for Tropical Storm 22W. 1800 UTC 07 October 2012 – 1200 UTC 08 October 2012, 0000 UTC 17 October 2012 – 1800 UTC 18 October 2012. [Available online at <http://www.woeurope.eu/cgi-app/tropicstorm?LANG=eu&GEBIET=sep&STURM=wp22&ADV=discus&ZEIT=201210072100>]
- , 2012: Prognostic Reasoning for Tropical Storm 24W. 0000 UTC 24 October 2012 – 0000 UTC 26 October 2012. [Available online at <http://www.woeurope.eu/cgi-app/tropicstorm?LANG=eu&GEBIET=sep&STURM=wp24&ADV=discus&ZEIT=201210240300>]
- , 2012: Prognostic Reasoning for Typhoon 16W. 0600 UTC 23 August 2012 – 1800 UTC 26 August 2012. [Available online at <http://www.woeurope.eu/cgi-app/tropicstorm?LANG=eu&GEBIET=sep&STURM=wp16&ADV=discus&ZEIT=201208242100>]

- , 2012: Prognostic Reasoning for Typhoon 17W. 0600 UTC 12 September 2012 – 1800 UTC 15 September 2012. [Available online at <http://www.woeurope.eu/cgi-app/tropicstorm?LANG=eu&GEBIET=sep&STURM=wp17&ADV=discus&ZEIT=201209122100>]
- , 2012: Prognostic Reasoning for Typhoon 18W. 1800 UTC 22 September 2012 – 0600 UTC 24 September 2012, 0000 UTC 28 September 2012 – 0600 UTC 29 September 2012. [Available online at <http://www.woeurope.eu/cgi-app/tropicstorm?CONT=euro&MAPS=euro&GEBIET=sep&STURM=wp18&ZEIT=201209230600&LANG=eu&ADV=discus>]
- , 2012: Prognostic Reasoning for Typhoon 22W. 0000 UTC 09 October 2012 – 0000 UTC 16 October 2012. [Available online at <http://www.woeurope.eu/cgi-app/tropicstorm?LANG=eu&GEBIET=sep&STURM=wp22&ADV=discus&ZEIT=201210112100>]
- , 2012: Prognostic Reasoning for Typhoon 24W. 1800 UTC 26 October 2012 – 0000 UTC 28 October 2012. [Available online at <http://www.woeurope.eu/cgi-app/tropicstorm?LANG=eu&GEBIET=sep&STURM=wp24&ADV=discus&ZEIT=201210271500>]
- , cited 2013: Frequently Asked Questions. [Available online at <http://www.usno.navy.mil/JTWC/frequently-asked-questions-1/frequently-asked-questions#labels>]
- Jones, S. C., and Coauthors, 2003: The extratropical transition of tropical cyclones: Forecast challenges, current understanding, and future directions. *Wea. Forecasting*, **18**, 1052–1092.
- Knaff et al., 2010: An evaluation of Dvorak technique-based tropical cyclone intensity estimates. *Wea. Forecasting*, **25**, 1362–1379.
- Kossin, J. P., and M. Sitkowski, 2009: An objective model for identifying secondary eyewall formation in hurricanes. *Mon. Wea. Rev.*, **137**, 876 – 892.
- , [J. A. Knaff, H. I. Berger, D. C. Herndon, T. A. Cram, C. S. Velden, R. J. Murnane, and J. D. Hawkins, 2007: Estimating hurricane wind structure in the absence of aircraft reconnaissance. *Wea. Forecasting*, **22**, 89–101.](#)
- Kuo, H. C., C. P. Chang, and H. J. Jiang, 2009: Western North Pacific typhoons with concentric eyewalls. *Mon. Wea. Rev.*, **137**, 3758–3770.

- Möller, J. D. and M. T. Montgomery, 1999: Vortex rossby waves and hurricane intensification in a barotropic model. *J. Atmos. Sci.*, **56**, 1674-1687.
- National Environmental Satellite, Data, and Information Service, cited 2012: What is TeraScan? [Available online at http://psbcw1.nesdis.noaa.gov/terascan/home_basic/what_is_terascan.html]
- Olander, T. L. and C. S. Velden, 2007: The Advanced Dvorak Technique: Continued development of an objective scheme to estimate tropical cyclone intensity using geostationary infrared satellite imagery. *Wea. Forecasting*, **22**, 287-298.
- and -----, 2009: Tropical cyclone convection and intensity analysis using differenced infrared and water vapor imagery. *Wea. Forecasting*, **24**, 1558-1572.
- Piñeros, M. F., E. A. Ritchie, G. Valliere-Kelley, and J. S. Tyo, 2011: Tropical cyclone intensity estimation in the north Atlantic basin using an improved deviation angle variance technique. *Wea. Forecasting*, **27**, 1264-1277.
- Qiu, X. and Z. M. Tan, 2010: The roles of vortex rossby waves in hurricane secondary eyewall formation. *Mon. Wea. Rev.*, **138**, 2092-2109.
- Riehl, H., 1948: On the formation of typhoons. *J. Meteor.*, **5**, 247-265.
- Shapiro, L. J., and H. E. Willoughby, 1982: The response of balanced hurricanes to local sources of heat and momentum. *J. Atmos. Sci.*, **39**, 378-394.
- Stern, D. P. and F. Zhang, 2012: How does the eye warm? Part I: A potential temperature budget analysis of an idealized tropical cyclone. *J. Atmos. Sci.*, **70**, 73-90.
- Velden, Christopher, and Coauthors, 2006: The Dvorak tropical cyclone intensity estimation technique: a satellite-based method that has endured for over 30 years. *Bull. Amer. Meteor. Soc.*, **87**, 1195-1210.
- Wilks, D. S., 1996: *Statistical Methods in the Atmospheric Sciences*. Elsevier Inc, 648 pp.
- Willoughby, H. E., J. A. Clos, and M. G. Shoreibah, 1982: Concentric eyewalls, secondary wind maxima, and the evolution of the hurricane vortex. *J. Atmos. Sci.*, **39**, 395 – 411.
- Wimmers, A. J. and C. S. Velden, 2010: Objectively determining the rotational center of tropical cyclones in passive microwave satellite imagery. *J. Appl. Meteorol. Clim.*, **49**, 2013-2.